Journal of Computational Physics 229 (2010) 4952–4979

Contents lists available at ScienceDirect

Journal of Computational Physics

journal homepage: www.elsevier.com/locate/jcp

# An accurate solver for forward and inverse transport

François Monard, Guillaume Bal *

*Department of Applied Physics and Applied Mathematics, Columbia University, New York, NY 10027, United States*

ARTICLE INFO

*Article history:*
Received 27 June 2009
Received in revised form 5 March 2010
Accepted 13 March 2010
Available online 17 March 2010

*Keywords:*
Radiative transport equations
Inverse transport
Numerical simulations of singular solutions
Numerical inversion of optical parameters

ABSTRACT

This paper presents a robust and accurate way to solve steady-state linear transport (radiative transfer) equations numerically. Our main objective is to address the inverse transport problem, in which the optical parameters of a domain of interest are reconstructed from measurements performed at the domain's boundary. This inverse problem has important applications in medical and geophysical imaging, and more generally in any field involving high frequency waves or particles propagating in scattering environments. Stable solutions of the inverse transport problem require that the singularities of the measurement operator, which maps the optical parameters to the available measurements, be captured with sufficient accuracy. This in turn requires that the free propagation of particles be calculated with care, which is a difficult problem on a Cartesian grid.

A standard discrete ordinates method is used for the direction of propagation of the particles. Our methodology to address spatial discretization is based on rotating the computational domain so that each direction of propagation is always aligned with one of the grid axes. Rotations are performed in the Fourier domain to achieve spectral accuracy. The numerical dispersion of the propagating particles is therefore minimal. As a result, the ballistic and single scattering components of the transport solution are calculated robustly and accurately. Physical blurring effects, such as small angular diffusion, are also incorporated into the numerical tool. Forward and inverse calculations performed in a two-dimensional setting exemplify the capabilities of the method. Although the methodology might not be the fastest way to solve transport equations, its physical accuracy provides us with a numerical tool to assess what can and cannot be reconstructed in inverse transport theory.



## 1. Introduction

The radiative transfer (linear Boltzmann or linear transport) equation finds applications in several areas of applied sciences such as e.g. nuclear reactors, atmospheric science and astrophysics, and medical imaging. The transport equation models the density of particles or the energy density of waves propagating in a scattering medium. In several of these applications, the ultimate objective is to solve an inverse transport problem rather than a forward transport problem. The inverse transport problem consists of reconstructing the constitutive parameters in the transport equation from available (typically boundary) measurements. In this paper, we refer to the constitutive parameters as the optical parameters. The operator mapping the optical parameters to the available measurements is called the measurement operator (or albedo operator). Our objective is to develop a numerical tool that allows us to understand what can and cannot be reconstructed from a given measurement operator and with what type of stability.

* Corresponding author. Tel.: +12128544731; fax: +12128548257.
*E-mail addresses:* fm2234@columbia.edu (F. Monard), gb2030@columbia.edu (G. Bal).

0021-9991/$ - see front matter © 2010 Elsevier Inc. All rights reserved.
doi:10.1016/j.jcp.2010.03.016

### 1.1. Transport regime of propagation

Many numerical tools have been developed to solve the transport equation; see e.g. [1,22,18,24,25]. Most are tailored to perform well in the regime of high scattering but do not necessarily adequately capture particle propagation in the regime of interest in this paper. The transport of particles may roughly be characterized by three regimes: (i) the regime of free transport (or ballistic regime), where particles do not interact with the underlying structure; (ii) the regime of moderate scattering (referred to as transport regime), where many but not all particles (statistically) interact with the underlying structure; and (iii) the diffusive regime, where scattering is overwhelming. We are interested here in the intermediate transport regime, where scattering cannot be neglected and in fact will be crucial for the inverse problem, but where a significant fraction of the propagating particles do not interact with the scattering medium. Such a regime is characterized by a mixture of singular behavior (particles with a given direction have a reasonable probability of keeping that direction until they exit the domain) and smoothing behavior (the distribution of particles becomes smoother as scattering occurs).

### 1.2. Singularities of the albedo operator

Theoretical results on the inverse transport problem show that the most stable reconstructions of the optical parameters require that the singularities of the measurement be captured accurately. This implies that the free transport of particles be calculated accurately. This is where most existing transport codes will be inaccurate because of almost inevitable numerical dispersion. Arguably no numerical method fails more miserably than the second-order diamond method [8] because high frequencies are neither accurately estimated nor damped numerically. Higher-order methods will see a much improved behavior though at the price of a significant unphysical (and typically uncontrolled) damping of high frequencies [26]. Nonlinear algorithms [17,23] or unstructured grids based on e.g. discontinuous Galerkin methods [19] might be used with their own limitations. We do not follow that route here.

In the regime of free transport (no scattering), the transport equation becomes an ordinary differential equation for which many accurate techniques are available. In the regime of fairly high scattering, as for instances in applications in nuclear reactor physics and in medical imaging in highly scattering media, such inaccuracies are not necessarily too important because sources may be relatively smooth and even when sources are not smooth, multiple scattering is accurately computed thanks to its regularizing effect.

In the intermediate regime of transport propagation, both the free propagation and scattering contributions need to be estimated accurately. Moreover, small scale physical blurring effects may need to be modeled accurately so that the effects of numerical dispersion need to be minimized as much as possible. Our methodology to do so is as follows.

### 1.3. Rotations

Because the transport solution is quite singular in the direction of propagation, the angular variable is best described by using a discrete ordinates method, which replaces the sphere of directions of propagations by a finite number of directions. The optical parameters are discretized by using a Cartesian grid, which is the natural pixel-by-pixel representation of pictures. The spatial discretization of the transport equation is performed by rotating the domain so that each discrete direction of propagation is aligned with one of the axes of the Cartesian grid. The rotation is performed in the Fourier domain by using a fast Fourier transform in order to preserve spectral accuracy of the optical coefficient after rotation. The method is based on the slant stack algorithm developed in [5,6] and used in [12] to solve the inverse attenuated Radon transform. This is the most expensive step of the algorithm. For an $N^d$ picture, where $N$ is the number of pixels in each dimension and $d$ is spatial dimension, the calculation of the free transport solution, which after rotation requires that one solve an equation of the form $\frac{du}{dx} + a(x)u = f$, requires $O(N^d)$ calculations. The calculation of the rotation is proportional to $N^d \log N$ and therefore significantly increases the computational cost of the method. However, the line integral of the coefficient $a(x)$ is calculated quite accurately independent of the direction of propagation, which is a necessary step toward obtaining an accurate numerical solution of the inverse transport problem.

The above method allows us to solve the ballistic part of transport accurately. Multiple scattering is then calculated by using a standard iterative source method, where scatterings of order $m+1$ are calculated iteratively from scatterings of order less $m$ by using the free transport solver described above. Because we are interested in the transport regime and not the diffusive regime in this paper, the iterative source method converges relatively rapidly and does not require any acceleration [2,20].

### 1.4. Physical blurring and ray effects

The methodology based on rotations is a convenient framework to add physical effects that are responsible for the blurring of the ballistic part. One such physical blurring is that caused by small-angle diffusion. Such an effect is quite pronounced in highly peaked forward scattering, which is significant in many applications in medical imaging and remote sensing (imaging of the atmosphere). Such a blurring is considered by implementing angular and spatial diffusion in the transverse variables to the main direction of propagation. Such effects are related to the Fermi pencil beam approximation to the Fokker Planck equations that model angular diffusion. The numerical method presented here allows us to accurately

capture such physical blurring effects, which are important to understand what can and cannot be reconstructed from available measurements.

A similar type of blurring may be used to combat the so-called ray effect. The ray effect is a numerical effect caused by the finite number of directions used in the scheme. A physically localized source emitting smoothly in the angular variable will emit radiation only along these privileged directions of propagation in the discrete scheme. It will thus generate radiation along a finite number of lines with many pixels receiving no radiation at all. Such numerical solutions are accurate in a weak sense (i.e., after averaging over a sufficiently large domain) but not point-wise. We show that the choice of an appropriate diffusion coefficient allows one to mitigate the ray effect although this comes at a high computational price.

### 1.5. Numerical inversion

Once the forward transport solutions are simulated, they may be used to reconstruct the optical parameters from knowledge of various measurement operators. We consider here the case of the full steady-state measurement operator, in which the transport solution is measured at the domain's boundary for all possible incoming radiation conditions. This measurement operator is known to uniquely determine the optical parameters and to do so with a good stability estimate [9,10,30,31]. We present an iterative algorithm that accurately reconstructs the optical parameters from the measurement operator in the simplified setting of a two-dimensional geometry and isotropic scattering. The methodology is presented for general, anisotropic, scattering coefficients and is independent of spatial dimension, although we demonstrate its effectiveness only in dimension $d = 2$ and with isotropic scattering in the section devoted to numerical simulations.

### 1.6. Outline

The rest of the paper is structured as follows. Section 2 recalls the basic ingredients about the forward and inverse transport problems that we need in the sequel. The numerical method is presented in detail in Section 3. The influence of physical blurring and of numerical blurring to address ray effects is covered in Section 4. Finally, Section 5 addresses the numerical reconstructions of the optical parameters in a two-dimensional setting and shows the accuracy and robustness of the method. Some conclusions are offered in Section 6.

## 2. Theoretical setting

This section recalls the results we need in the sequel on the forward and inverse transport problem. The methodology generalizes without serious complications to the case of particles propagating with different energies or wavenumbers. To simplify the presentation, we assume for the rest of the paper that particles propagate with speed one so that the space of velocities is the space of directions of propagation.

### 2.1. Forward transport equation

Let $X$ be a convex bounded domain in $\mathbb{R}^d$, where $d$ is spatial dimension and $d = 2$ or $d = 3$ in practical applications. Let $\mathbb{S}^{d-1}$ be the unit sphere in $\mathbb{R}^d$. The transport equation we consider in this paper takes the form

$$\begin{aligned} &v \cdot \nabla_x u + \sigma(x, v)u = \int_{\mathbb{S}^{d-1}} k(x, v', v)u(x, v')dv', \quad \text{in } X \times \mathbb{S}^{d-1}, \\ &u(x, v) = g(x, v), \quad \text{on } \Gamma_-. \end{aligned} \tag{1}$$

Here, $u(x, v)$ is the density of particle at $x \in X$ propagating with direction $v \in \mathbb{S}^{d-1}$. The sets of incoming conditions $\Gamma_-$ and outgoing conditions $\Gamma_+$ are defined by

$$\Gamma_\pm = \Gamma_\pm(X) = \left\{(x, v) \in \partial X \times \mathbb{S}^{d-1}, \text{ s.t. } \pm v \cdot \nu(x) > 0\right\}, \tag{2}$$

where $\nu(x)$ is the outgoing normal vector to $X$ at $x \in \partial X$, the boundary of $X$. The source of incoming radiation $g(x, v)$ is prescribed on $\Gamma_-$.

The interactions of the particles with the underlying medium are described by the optical parameters $\sigma(x, v)$, the total attenuation, and $k(x, v', v)$, the scattering coefficient, which measures the probability of scattering from direction $v$ to direction $v'$ at a point $x$. In practical settings, $\sigma(x, v)$ is the sum of the scattering contribution $\sigma_p(x, v) = \int_{\mathbb{S}^{d-1}} k(x, v', v)dv'$ and of the intrinsic attenuation $\sigma_a(x, v)$. When the intrinsic attenuation is non-negative, the above Eq. (1) admits a unique solution in appropriate functional settings [9,15,16,27].

Moreover, the solution admits a convenient expression in terms of multiple scattering contributions. We define the times of escape of free-moving particles from $X$ as

$$\tau_\pm(x, v) = \inf\{s > 0 | x \pm sv \notin X\}, \tag{3}$$

and the operators

$$\mathcal{I}g(x,v) = \exp\left(-\int_0^{\tau_-(x,v)} \sigma(x-sv,v)ds\right) g(x-\tau_-(x,v)v,v), \tag{4}$$

$$\mathcal{K}u(x,v) = \int_0^{\tau_-(x,v)} \exp\left(-\int_0^t \sigma(x-sv,v)ds\right) \int_{\mathbb{S}^{d-1}} k(x-tv,v',v)u(x-tv,v')dv'\,dt. \tag{5}$$

We verify that $u_0(x,v) = \mathcal{I}g(x,v)$, which is called the ballistic part, solves (1) when $k \equiv 0$. We may then define $u_{n+1} = \mathcal{K}u_n$ for $n \geqslant 0$ and obtain that

$$u = \sum_{n\geqslant 0} u_n = \sum_{n\geqslant 0} (\mathcal{K})^n \mathcal{I}g(x,v) = (I-\mathcal{K})^{-1}\mathcal{I}g(x,v), \tag{6}$$

solves (1). The term $u_n(x,v)$ is the component of $u(x,v)$ that has scattered exactly $n$ times (i.e., is a homogeneous polynomial of degree $n$ in the scattering coefficient $k$).

When the spectral radius $\rho(\mathcal{K})$ of the operator $\mathcal{K}$ is not too large (i.e, bounded significantly away from 1), then the above series expansion, which is called the source iteration method, converges rapidly as $n \to \infty$. This is the case in the transport regime of propagation we are interested in this paper, where intrinsic attenuation is not negligible and where the optical depth of the domain of interest is not too large.

When $\rho(\mathcal{K})$ is close to 1, which occurs in the diffusive regime, diffusion accelerations of the method become necessary [2,20]. It should be relatively straightforward to accelerate the convergence of the source iteration method for the spatial discretization we propose below or to use alternative preconditioners to the diffusion acceleration as in e.g. [18,25]. This is not considered further here.

### 2.2. Albedo operator and inverse transport

The albedo or measurement operator is defined here as the operator mapping the incoming radiation to the transport solution $u_{|\Gamma_+}$ restricted at the domain's boundary: $\mathcal{A} : g \mapsto \mathcal{A}g = u_{|\Gamma_+}$. The albedo operator $\mathcal{A} \equiv \mathcal{A}[\sigma,k]$ depends on the optical parameters and may then be seen as an operator mapping the unknown optical parameters to the measurements of interest, which here are all possible couples $(g, u_{|\Gamma_+})$ on $\Gamma_- \times \Gamma_+$.

The theory of the reconstruction of the optical parameters from knowledge of $\mathcal{A}$ is well developed. We refer the reader to e.g. [9,10,15,30,31]. Stable reconstruction of the optical parameters is based on capturing the singularities in the albedo operator $\mathcal{A}$ as faithfully as possible. More precisely, we have that

$$\mathcal{A}g = \mathcal{I}g|_{\Gamma_+} + \mathcal{K}\mathcal{I}g|_{\Gamma_+} + \mathcal{K}^2(I-\mathcal{K})^{-1}\mathcal{I}g|_{\Gamma_+} := \mathcal{A}_0 g + \mathcal{A}_1 g + \mathcal{A}_2 g, \tag{7}$$

where $\mathcal{A}_0 g$ correspond to measurements of the ballistic part $u_0$, $\mathcal{A}_1 g$ to measurements of the single scattering part $u_1$, and $\mathcal{A}_2 g$ to measurements of the multiple scattering. Of course, $\mathcal{A}_0$ and $\mathcal{A}_1$ are not directly measurable. They have to be extracted from $\mathcal{A}$ and this is done by singularity analysis. In some sense, $\mathcal{A}_0$ is more singular than $\mathcal{A}_1$, which itself is more singular (in dimension $d \geqslant 3$, and in a much weaker sense in dimension $d = 2$) than $\mathcal{A}_2$. These singularities allow us to infer $\mathcal{A}_0$ and $\mathcal{A}_1$ from knowledge of $\mathcal{A}$. Let us denote the kernels of $\mathcal{A}_k$ by $\alpha_k$, i.e.,

$$\mathcal{A}_k g(x,v) = \int_{\Gamma_-} \alpha_k(x,v,y,v')g(y,v')d\mu(y)dv', \quad (x,v) \in \Gamma_+, \tag{8}$$

where $d\mu(y)$ is the surface measure on the boundary $\partial X$. Then we find that [10,15]

$$\alpha_0(x,v,y,v') = \exp\left(-\int_0^{\tau_-(x,v)} \sigma(x-sv,v)ds\right)\delta_v(v')\delta_{\{x-\tau_-(x,v)v\}}(y), \tag{9}$$

where $\delta_{\{x\}}$ is the delta function on the surface $\partial X$ defined by $\int_{\partial X} \delta_{\{x\}}(y)\phi(y)d\mu(y) = \phi(x)$ for $x \in \partial X$ and $\phi$ continuous on $\partial X$ and $\delta_v(v')$ is defined similarly on $\mathbb{S}^{d-1}$; and

$$\alpha_1(x,v,y,v') = \int_0^{\tau_-(x,v)} \exp\left(-\int_0^t \sigma(x-sv,v)ds - \int_0^{\tau_-(x-tv,v')} \sigma(x-tv-sv',v')ds\right) k(x-tv,v',v)\delta_{\{x-tv-\tau_-(x-tv,v')v'\}}(y)dt. \tag{10}$$

In other words, $\alpha_0$ uniquely defines the line integral of $\sigma$ along the line of direction $v$ passing through $x$. When $\sigma = \sigma(x)$ independent of $v$, this information uniquely characterizes $\sigma$ by means of an inverse Radon transform [28]. Once $\sigma(x)$ is known, then $\alpha_1$ uniquely characterizes $k(x,v',v)$. This is because when the lines $\{x - tv,\ t \in \mathbb{R}\}$ and $\{y + \tau v',\ \tau \in \mathbb{R}\}$ cross and $v \neq v'$, then $x - tv = y + \tau v' = \tau_-(x - tv, v')v'$ uniquely determines $t$ in (10).

We thus observe that the singular components of $\mathcal{A}$ allow us to uniquely (and stably) reconstruct $\sigma(x)$ and $k(x,v',v)$. Moreover the stability analyses in [10,15,30,31] show that $\mathcal{A}_0$ and $\mathcal{A}_1$ can indeed be extracted from knowledge of $\mathcal{A}$ in a stable manner. We refer the reader to the aforementioned literature and the topical review [9] for more information on this technical topic.

Note that $\alpha_k$ in (9) and (10) is obtained by formally setting $g(y,v') = \delta_{\{y_0\}}(y)\delta_{v_0}(v')$ in (8). In other words, the singular structure of the albedo operator is obtained by solving (1) with singular boundary conditions on $\Gamma_-$ and measuring the singular structure of the solution $u$ on $\Gamma_+$. This is the main task for the numerical method that is presented below.

## 3. Numerical method

We now present in detail the numerical method that we use to solve (1). The source iteration method requires that we solve problems of the form

$$\begin{aligned} &v\cdot\nabla_x u + \sigma(x)u = f(x,v), \quad \text{in } X\times\mathbb{S}^{d-1},\\ &u(x,v) = g(x,v), \quad \text{on } \Gamma_-, \end{aligned} \tag{11}$$

where the volume source term $f(x,v)$ takes for instance the form

$$f(x,v) = Ku_n(x,v) := \int_{\mathbb{S}^{d-1}} k(x,v',v)u_n(x,v')dv', \tag{12}$$

in the calculation of $u_{n+1}(x,v)$. We assume here that $\sigma = \sigma(x)$ to simplify since this is the setting of interest for the inverse problem.

The above problems are uncoupled in the variable $v$. Let some $v$ be fixed. The main practical difficulty in solving (11) numerically is that the optical coefficients, and hence the source term $f(x,v)$, are defined on a grid, here a Cartesian grid, independent of $v$. As we mentioned in the introduction, solving the hyperbolic problem (11) on a Cartesian grid is a challenge in spite of the apparent simplicity of the (hyperbolic) equation. Our strategy is based on performing a rotation of the computational domain so that the main direction of propagation becomes aligned with one of the grid axes.

### 3.1. Geometrical setting

The proposed method is essentially independent of spatial dimension. To simplify the presentation and because this is what has been implemented so far, we restrict ourselves to the two-dimensional setting $X = B(0,1)\subset\mathbb{R}^2$, where $B(0,1)$ is the centered ball of radius unity. The choice of $X$ is such that the domain where $\sigma$ and $k$ are supported is invariant by rotation. The computational domain however is made $v$-dependent as follows. We now denote $v = v(\theta) = (\cos\theta,\sin\theta)\in\mathbb{S}^1$, where $\theta\in(0,2\pi)$, and $v^\perp = v(\theta)^\perp$ is the (counterclockwise) rotation of $v$ by 90 degrees, that is $v(\theta)^\perp = (-\sin\theta,\cos\theta)$. For any function $f(v)$ defined on $\mathbb{S}^1$, we define the function $f(\theta) := f(v(\theta))$ on $(0,2\pi)$ and use the same symbol $f$ for both functions.

For each $\theta\in(0,2\pi)$, we define the $\theta-$ dependent square as

$$C_\theta = \{x\in\mathbb{R}^2 \text{ such that } |x\cdot v|<1 \text{ and } |x\cdot v^\perp|<1\}. \tag{13}$$

The incoming and outgoing sets for such a domain are given by

$$\Gamma_{\pm,\theta} = \{x\in\partial C_\theta \text{ such that } x\cdot v = \pm 1 \text{ and } |x\cdot v^\perp|<1\}. \tag{14}$$

See Fig. 1. This geometry is quite practical since it corresponds for each $\theta\in(0,2\pi)$ to an array of sources emitting radiation from the segment (square when $d=3$) $\Gamma_{-,\theta}$ and an array of detectors present also on the segment (square when $d=3$) $\Gamma_{+,\theta}$.

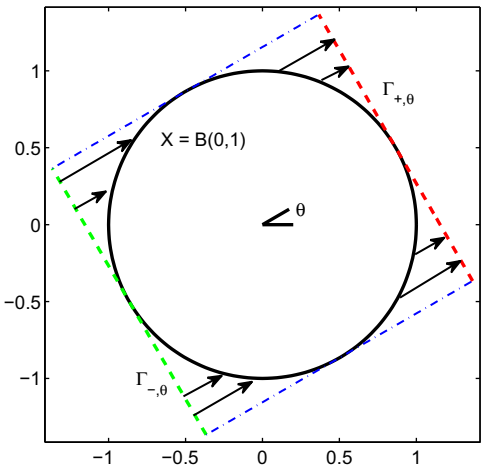


**Fig. 1.** A square $C_\theta$. The arrows indicate how incoming boundary conditions on $\Gamma_{-,\theta}$ are mapped to the boundary of the unit disk and how outgoing measurements are measured on $\Gamma_{+,\theta}$.

Since scattering and attenuation vanish outside of $X = B(0,1)$, it is not difficult to map incoming and outgoing conditions from $\Gamma_\pm(X)$ as it was defined in (2) to incoming and outgoing conditions on $\Gamma_{\pm,\theta}$ as they are defined in (14).

Let us freeze $\theta$ and define, for $x = (x,y) \in [-1,1]^2$, and given functions $u$ on $\mathbb{R}^2 \times (0,2\pi)$ and $w$ on $\mathbb{R}^2$,

$$u_\theta(x,y) \equiv [u]_\theta(x,y) := u(x\cos\theta - y\sin\theta, x\sin\theta + y\cos\theta, \theta),$$
$$w_\theta(x,y) \equiv [w]_\theta(x,y) = w(x\cos\theta - y\sin\theta, x\sin\theta + y\cos\theta).$$

(We will use the bracket notation whenever $u$ or $w$ already have lower indices.) Note that $u_\theta$ and $w_\theta$ are the reparameterizations along the axes $v$ and $v^\perp$ of $u|_{C_\theta}$ and $w|_{C_\theta}$ and that both are supported in $X = B(0,1)$. We now verify that (11) can be rewritten as the following ordinary differential equation (ODE) for $u_\theta$:

$$\begin{aligned} &\frac{d}{dx}u_\theta(x,y) + \sigma_\theta(x,y)u_\theta(x,y) = f_\theta(x,y), \quad (x,y) \in C_\theta, \\ &u_\theta(-1,y) = \tilde{g}_\theta(y), \quad \text{on } \Gamma_{-,\theta}, \end{aligned} \tag{15}$$

where $\tilde{g}_\theta$ is obtained by projecting the input $g(\cdot,\theta)$ supported on the set $\{x, (x,\theta) \in \Gamma_-\}$ back onto $\Gamma_{-,\theta}$. Formally, we have that $\tilde{g}_\theta = g\left(P_-^{-1}(\cdot,\theta)\right)$, where we have defined the projection operators

$$P_\pm : \Gamma_\pm \ni (x,\theta) \mapsto P_\pm(x,\theta) = \pm v(\theta) - \det(x, v(\theta))\, v(\theta)^\perp \in \Gamma_{\pm,\theta}. \tag{16}$$

When solving Eq. (15), the measurements we collect on $\Gamma_{+,\theta}$ are expressed as

$$u_\theta|_{\Gamma_{+,\theta}} = u|_{\Gamma_+}\left(P_+^{-1}(\cdot,\theta)\right).$$

Eq. (15) is what we solve in practice: we first compute $\sigma_\theta$ and $f_\theta$ by rotating the images of $\sigma$ and $f(\cdot,\theta)$ clockwise by an angle $\theta$, next solve (15) for $u_\theta$ on a Cartesian grid in (x,y), and finally rotate the image of $u_\theta$ (i.e., we compute $[u_\theta]_{-\theta}$) back to a Cartesian grid aligned with the original frame $(e_x, e_y)$.

In order to simulate the albedo operator $\mathcal{A}$, we thus need to solve problems of the form (11) with $g(x,\theta) = \delta(x - x_0)$ for $x_0$ an arbitrary point in $\Gamma_{-,\theta}$ and with $f(x,\theta)$ a source term of the form prescribed above, where $u_n(x,\theta)$ is the solution after $n$ scattering iterations of the problem (1) (involving all directions of propagation) with a boundary condition on $\Gamma_-(X)$ of the form $g(x,\theta) = \delta_{\{x_0\}}(x)\delta_{\theta_0}(\theta)$.

### 3.2. Discrete ordinates and iterative source method

The numbers of directions of propagation $N_d$ in (11) needs to be finite in practice. The directions are chosen uniformly distributed on the unit circle. This is the standard discrete ordinates method to solve (1). Once the number of directions is chosen, the integral on the right-hand side in (1) also needs to be discretized.

To this end, we define the angular step-size $\delta := \frac{2\pi}{N_d}$, as well as the sets $\Theta_\delta = \{\theta_1, \ldots, \theta_{N_d}\}$ and $\mathbb{S}^1_\delta = \{v_1, \ldots, v_{N_d}\}$, where for each $i = 1, \ldots, N_d$, $\theta_i = \left(i - \frac{1}{2}\right)\delta$ and $v_i = (\cos\theta_i, \sin\theta_i)$. For a function $f$ defined on $X \times \Theta_\delta$, we define on $X \times \Theta_\delta$ the function

$$K_\delta f(x,\theta_i) = \delta \sum_{j=1}^{N_d} f(x,\theta_j)k(x,\theta_j,\theta_i), \quad x \in X,\ i = 1, \ldots, N_d. \tag{17}$$

With the new notation and operators, the semi-discretized problem in order to compute the $n$th scattering term reads

$$\begin{aligned} &v \cdot \nabla_x u_n(x,\theta) + \sigma(x)u_n(x,\theta) = K_\delta u_{n-1}(x,\theta), \quad \text{in } X \times \Theta_\delta, \\ &u_n(x,\theta_i) = g(x,\theta_i), \quad \text{on } \Gamma_{-,\theta_i},\ i = 1, \ldots, N_d, \end{aligned} \tag{18}$$

where, by convention for $n = 0$, $K_\delta u_{-1} = 0$. In our geometrical setting, we rewrite the system of equations (18) as follows:

$$\begin{aligned} &\frac{d}{dx}[u_n]_{\theta_i} + \sigma_{\theta_i}[u_n]_{\theta_i} = [K_\delta u_{n-1}]_{\theta_i}, \quad \text{on } C_{\theta_i},\ i = 1, \ldots, N_d, \\ &[u_n]_{\theta_i}(-1,y) = \tilde{g}_{\theta_i}(y), \quad \text{on } \Gamma_{-,\theta_i},\ i = 1, \ldots, N_d. \end{aligned} \tag{19}$$

Let us denote by $N_{scat}$ the number of scattering terms we want to solve for numerically (this can be replaced by a criterion stopping the calculation whenever a given accuracy is attained by the iterative scheme). A schematic presentation of the forward transport code when scattering is isotropic is given by Algorithm 1.

**Algorithm 1.** Forward transport solver (case of isotropic scattering).

Prescribe boundary conditions and optical parameters $\{\tilde{g}_{\theta_i}\}_{i=1}^{N_d}, \sigma, k$;
{Computation of the ballistic part}
**for** $i = 1$ to $N_d$ **do**
  compute $\sigma_{\theta_i}$ by rotation;
  solve for $[u_0]_{\theta_i}$ the equation

$$\frac{d}{dx}[u_0]_{\theta_i} + \sigma_{\theta_i}[u_0]_{\theta_i} = 0, \quad \text{on } C_{\theta_i},$$
$$[u_0]_{\theta_i}|_{\Gamma_{-,\theta_i}} = \tilde{g}_{\theta_i}, \quad \text{on } \Gamma_{-,\theta_i};$$

  compute $[[u_0]_{\theta_i}]_{-\theta_i}$ by rotation as an approximation of $u_0(\cdot, \theta_i)$;
**end for**
{Computation of the scattering terms}
**for** $n = 1$ to $N_{\text{scat}}$ **do**
  compute the source term $f_n := K_\delta u_{n-1}$;
  **for** $i = 1$ to $N_d$ **do**
    compute $\sigma_{\theta_i}$ and $[f_n]_{\theta_i}$ by rotation;
    solve for $[u_n]_{\theta_i}$ the equation

$$\frac{d}{dx}[u_n]_{\theta_i} + \sigma_{\theta_i}[u_n]_{\theta_i} = [f_n]_{\theta_i}, \quad \text{on } C_{\theta_i},$$
$$[u_n]_{\theta_i}|_{\Gamma_{-,\theta_i}} = \tilde{g}_{\theta_i}, \quad \text{on } \Gamma_{-,\theta_i};$$

    compute $[[u_n]_{\theta_i}]_{-\theta_i}$ by rotation as an approximation of $u_n(\cdot, \theta_i)$;
  **end for**
**end for**

This algorithm requires image rotations and solutions of ordinary differential equations. We now describe how these operations are performed.

### 3.3. Rotation of the computational domain and ODE solver

The salient feature of the paper is the way we solve the free transport Eq. (11) by using rotations. We rewrite it as (15), where the computation of $\sigma_\theta$ and $f_\theta$ requires the computational domain to be rotated in such a way that the $v$-axis becomes one of the axes $\pm e_x$ or $\pm e_y$ of the Cartesian grid. We then solve the ODE on this grid and rotate the computed solution back to the initial grid. Hence the two elementary functions are the image rotation and the ODE solver on a Cartesian grid, which we now describe in detail.

The square $[-1,1]^2$ is discretized into $n \times n$ equispaced points of coordinates

$$\mathrm{x} \otimes \mathrm{y} = \{(\mathrm{x}(i), \mathrm{y}(j))\}_{i,j=1}^{n}, \quad \text{where } \mathrm{x}(j) = \mathrm{y}(j) = -1 + \frac{1}{n} + (j-1)\frac{2}{n}. \tag{20}$$

This grid is centered at 0, and rotations are performed to keep 0 invariant.

#### 3.3.1. Image rotation

We now want to rotate an $n$-by-$n$ image by an angle $\theta$. The image represents the values of a mapping over the grid $\mathrm{x} \otimes \mathrm{y}$ defined in (20). The mapping is further assumed to be supported in $X$. The main idea is to realize a rotation by means of image shearing (slanting) and dilation, successively along the columns and rows of the image. Each operation is performed in the Fourier domain using a fast Fourier transform to preserve spectral accuracy.

We describe the rotation technique for $\theta \in [0, \frac{\pi}{4}]$. For other values of $\theta$, we use rotations by $\frac{\pi}{2}$ and reflections about the axis $e_y$ (which are simple re-indexing exercises) to bring $\theta$ into the interval $[0, \frac{\pi}{4}]$. We decompose the rotation function $r_\theta : \mathbb{R}^2 \to \mathbb{R}^2$ defined by

$$r_\theta : (\mathrm{x}, \mathrm{y}) \mapsto r_\theta(\mathrm{x}, \mathrm{y}) = (\mathrm{x}\cos\theta + \mathrm{y}\sin\theta, -\mathrm{x}\sin\theta + \mathrm{y}\cos\theta), \tag{21}$$

as a product of four Cartesian-friendly operations. This decomposition can be achieved by the following composition of elementary functions:

$$
\begin{aligned}
&r_\theta = d_{\mathrm{x},\frac{1}{\cos\theta}} \circ s_{\mathrm{x},-\sin\theta} \circ d_{\mathrm{y},\cos\theta} \circ s_{\mathrm{y},\tan\theta}, \quad \text{where for } (\mathrm{x},\mathrm{y}) \in \mathbb{R}^2,\\
&s_{\mathrm{y},\alpha}(\mathrm{x},\mathrm{y}) = (\mathrm{x}, \mathrm{y} - \alpha\mathrm{x}), \quad \alpha \in \mathbb{R}, \qquad s_{\mathrm{x},\beta}(\mathrm{x},\mathrm{y}) = (\mathrm{x} - \beta\mathrm{y}, \mathrm{y}), \quad \beta \in \mathbb{R},\\
&d_{\mathrm{x},t}(\mathrm{x},\mathrm{y}) = (t\mathrm{x}, \mathrm{y}), \quad t \in \mathbb{R}, \qquad d_{\mathrm{y},t}(\mathrm{x},\mathrm{y}) = (\mathrm{x}, t\mathrm{y}), \quad t \in \mathbb{R}.
\end{aligned} \tag{22}
$$

The $s$ operators are slant (shearing) operators, where the first index indicates the axis that is parallel to shearing and the second gives the rate of shearing: $s_{\mathrm{y},\tan\theta}$ aligns the axis $(0, v(\theta))$ with the axis $(0, e_{\mathrm{x}})$. This slant induces a vertical stretching that is compensated by the vertical homothecy $d_{\mathrm{y},\cos\theta}$. Then the horizontal shearing $s_{\mathrm{x},-\sin\theta}$ aligns the axis $(0, v(\theta)^{\perp})$ with $(0, e_{\mathrm{y}})$, inducing a horizontal stretching that is compensated by the horizontal homothecy $d_{\mathrm{x},-\sin\theta}$. Numerically, the shearing uses the 'slanting' technique, in which we embed the image in a bigger image and slant it. The homothecy (dilation) is achieved by a resampling done in the Fourier domain with spectral accuracy of the sheared image, which brings it back to its original size. Fig. 2 illustrates how these steps are combined to execute an image rotation. These two steps are now spelled out in detail.

### 3.3.2. Vertical shearing

We now explain how to shear, or 'slant' an image vertically. Horizontal shearing is performed similarly. The idea behind vertical slant is to shift each column of the image independently with a shift that increases linearly with the column index at rate $-t$. This produces a globally sheared image, in which lines with slope $t$ become horizontal.

In order to avoid that the upper-left and lower-right corners of the image share a common row in the sheared image, we embed the $n$-by-$n$ image into a $2n$-by-$n$ image prior to shearing. We do this by adding $\frac{n}{2} \times n$ arrays of zeros above and below the image, which allows for shearing of angles $\theta \leqslant \frac{\pi}{4}$. This non-overlapping condition is important in order to perform the shearing in the Fourier domain after periodization of the image.

The operation of shifting a vector $x = [x_1, \ldots, x_n]^T$ by a shift $s$ is done as follows. We first define the $2n$-periodic function

$$
D_n(\mathrm{y}) = \frac{\sin(\pi\mathrm{y})}{n \sin\left(\frac{\pi\mathrm{y}}{n}\right)}, \quad \mathrm{y} \in \mathbb{R}, \tag{23}
$$

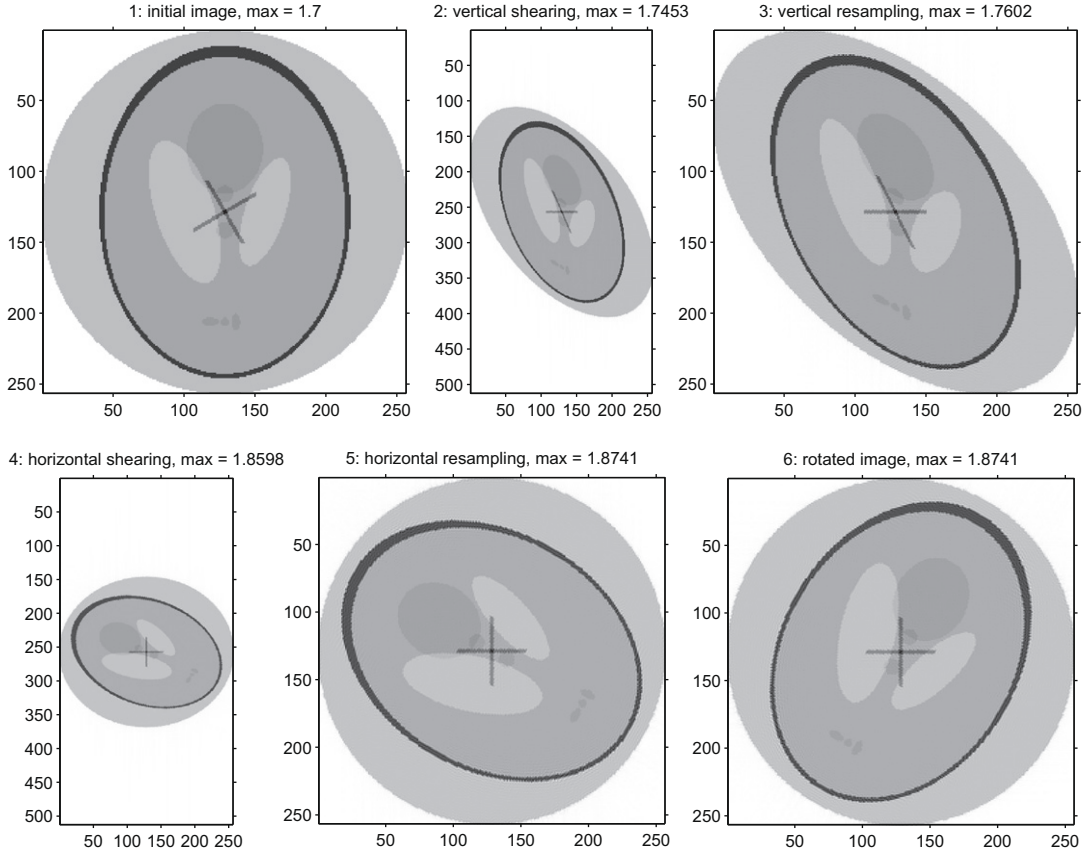


**Fig. 2.** The steps involved in an image rotation by $\theta = \frac{\pi}{6}$. We use the Shepp–Logan phantom with a cross superimposed at its center to indicate which axis is straightened during each of the shearing steps. By looking at maximum values of the pixels, we observe that the spectral rotations create overshoots and oscillations near discontinuities as a standard manifestation of the Gibb's phenomenon.

and assume that $x$ represents the values of a mapping on a grid $\mathrm{y}_1, \ldots, \mathrm{y}_n$ of step-size 1. Now we define the $n$-periodic continuous interpolant of $x$ as $\tilde{x}(\mathrm{y}) = \sum_{i=1}^{n} x_j D_n(\mathrm{y} - j)$, and the resulting shifted vector is defined as

$$x_s = [\tilde{x}(1+s), \ldots, \tilde{x}(n+s)]^T.$$

Numerically, the operation of spectral shifting consists of a convolution of the initial vector $x$ with $\{D_n(j+s)\}_{j=1}^{n}$. This can be done in $\mathcal{O}(n \log n)$ operations using the Fast Fourier Transform (FFT) algorithm. We recall the $N$-point Discrete Fourier Transform (DFT) and its inverse (IDFT) are defined as:

$$\begin{aligned} X(k) &= F^{N}_{j \mapsto k}[x(j)] = \sum_{j=1}^{N} x(j) e^{-\frac{2i\pi}{N}(j-1)(k-1)}, \quad k = 1, \ldots, N, \\ x(j) &= F^{-1,N}_{k \mapsto j}[X(k)] = \frac{1}{N} \sum_{k=1}^{N} X(k) e^{\frac{2i\pi}{N}(j-1)(k-1)}, \quad j = 1, \ldots, N. \end{aligned} \tag{24}$$

Because of the vertical zero-padding mentioned earlier, we now assume that $N = 2n$ and that our vectors represent $N$-periodic functions on a grid $y_1, \ldots, y_N$ of step-size 1. The shift $s$ is scaled on the interval $[0, N]$, and we will make use of the following interpolating function

$$D_{2n}(t) = \frac{\sin(\pi t)}{2n \sin\frac{\pi t}{2n}} = \frac{1}{2n} \sum_{k=-n}^{n-1} e^{\frac{i\pi}{n}\left(k+\frac{1}{2}\right)t}, \quad t \in [0, 2n].$$

Now the spectral interpolant of $x$ is given by $\tilde{x}(y) = \sum_{j=1}^{2n} x(j) D_{2n}(y - j)$, and looking at the function $x_1(y) = \tilde{x}(y - s)$ on the initial grid, expanding $D_{2n}$ as a sum of complex exponentials and using the definition (24), we obtain after some algebra:

$$x_1(y_l) = e^{\frac{i\pi}{n}\left(-n+\frac{1}{2}\right)(l-1)} F^{-1,2n}_{k \mapsto l}\left[ e^{-\frac{i\pi}{n}\left(k-1-n+\frac{1}{2}\right)s} F^{2n}_{j \mapsto k}\left[ x(j) e^{-\frac{i\pi}{n}\left(-n+\frac{1}{2}\right)(j-1)} \right] \right], \quad l = 1, \ldots, 2n. \tag{25}$$

Using the $N = 2n$ variable, Eq. (25) reads:

$$x_1(y_l) = e^{\frac{i\pi}{N}(-N+1)(l-1)} F^{-1,N}_{k \mapsto l}\left[ e^{-\frac{i\pi}{N}(2k-2-N+1)s} F^{N}_{j \mapsto k}\left[ x(j) e^{-\frac{i\pi}{N}(-N+1)(j-1)} \right] \right], \quad l = 1, \ldots, N. \tag{26}$$

This is how we have implemented the shift function with the `FFT` and `IFFT` functions.

### 3.3.3. Resampling

Now we want to resample each column with a different step-size in order to compensate for the stretching effect induced by the image shearing and bring the image back to its original size. In order to do that, we work again with the spectral interpolating function $D_{2n}$ and pick values of the interpolated columns at new gridpoints. In our case, we want to resample a vector $x$ of size $N = 2n$ down to a vector $x_1$ of size $n$ with a different step-size. Assume that the vector $x$ takes values at the gridpoints $\{j-1\}_{j=1}^{2n}$ and the vector $x_1$ takes values at $y_l = s + h(l-1)$, $l = 1, \ldots, n$, with $h \leqslant 1$ and $s$ fixed. The interpolant of $x$ is, again, defined with the function $D_{2n}$, and a similar calculation to (26) gives

$$x_1(y_l) = \frac{1}{N} e^{\frac{i\pi}{N}(-N+1)h(l-1)} G^{N,-\frac{h}{N}}_{k \mapsto l}\left[ e^{\frac{i\pi}{N}(2k-N-2+1)s} F^{N}_{j \mapsto k}\left[ x(j) e^{-\frac{i\pi}{N}(-N+1)(j-1)} \right] \right], \tag{27}$$

where the operator $G^{N,\alpha}$ is a $N$-point fractional Fourier transform of coefficient $\alpha$ (see [7]):

$$X(l) = G^{N,\alpha}_{k \mapsto l}[x] = \sum_{k=1}^{N} x(k) e^{-i2\pi\alpha(k-1)(l-1)}. \tag{28}$$

In order to compute this transform with $\mathcal{O}(n \log n)$ complexity, we implemented the "chirp $z$-transform" technique described in [7]. This technique allows us to express (28) as a $2N$-point circular convolution, which can then be computed with FFT's and IFFT's, hence with a complexity of order $\mathcal{O}(N \log N)$.

### 3.3.4. Complexity

As we have seen, the image rotation function is a succession of FFT's, IFFT's and fractional Fourier transforms of computational complexity $\mathcal{O}(2n \log(2n))$ and component-wise multiplications of computational complexity $\mathcal{O}(2n)$, applied for each column or each row (i.e., $n$ times). Hence for an $n$-by-$n$ image, the overall computational cost is of order $\mathcal{O}(n^2 \log n)$.

### 3.3.5. ODE solver

Every time we rotate images into the appropriate grid, we then need to solve an ODE on this grid. Our equations have the form

$$\frac{\partial u}{\partial \mathrm{x}}(\mathrm{x}, \mathrm{y}) + a(\mathrm{x}, \mathrm{y}) u(\mathrm{x}, \mathrm{y}) = f(\mathrm{x}, \mathrm{y}), \tag{29}$$

and need to be solved on the grid $\mathrm{x} \otimes \mathrm{y}$ defined in (20), with initial conditions set on the side {$x$=-1}. In order to solve this ODE, we use a finite difference scheme, marching along the columns from the incoming boundary {$x$=-1} to the outgoing

boundary $\{x=1\}$. We have restricted ourselves to the simplest of schemes here, namely the Explicit Euler scheme. We have done so here to demonstrate that capturing the location of singularities (here, delta functions in angle and space) is more important than capturing their amplitude with high accuracy. Higher-order schemes (e.g. Adams–Bashforth method) may obviously be considered as well and would be easily implementable in the context of the method presented here.

#### 3.3.6. A note on resampling

Note that the slant $s_{y,\tan\theta}$ in the rotation in (22) maps the line with slope $\theta$ onto the x-axis and thus also maps (11) to an ODE of the form (29). The above ODE is therefore not affected by the other steps involved in the rotation as in the references [5,6,12]. If we were only interested in solving the above ODE and the radiative transfer Eq. (1), then the slanting step alone would be sufficient. Though still of complexity $O(n^2 \log n)$, the computational cost would be significantly reduced by not performing the second slant and the two homothecies. We will see below that the full rotation allows for a simple accounting of noise effects such as the highly peaked forward scattering effect, which is difficult to handle by only shearing the images. The ray effect treated below is also more easily handled after full rotation of the computational domain. This is the reason why we have presented the setting with full rotations. Again, only one slant $s_{y,\tan\theta}$ is sufficient to solve (11), and hence (1), by a Cartesian-friendly method. The treatment of the incoming boundary conditions, however, needs to be addressed with some care and slightly differently from what we are doing here in the framework of full rotations. We do not consider this difficulty here.

### 3.4. Computational results for ballistic and single scattering parts

As advertised earlier, the main advantage of the method developed in this paper is that it allows us to estimate the singularities of the transport solution with reasonable accuracy. In order to find the limitations of the method, it is worth looking at how such a singularity is shifted by the spectral method during rotation. Like any Fourier-based method, this method conserves the high frequency content of the initial singularity and we thus expect some oscillations on the resulting image. Let $s$ be the value of the shift and $h$ the step-size of the grid. A good indicator is how well the method does versus the quantity $\mathrm{mod}(s,h)$ ($s$ modulo $h$). See Fig. 3.

#### 3.4.1. Effects of spectral shifts and slants

When $\mathrm{mod}(s,h)=0$, the singularity is shifted by an integer number of grid points and is thus exact. In every other case, shifting a singularity to a location between two gridpoints (the case $\mathrm{mod}(s,h)\neq 0$) creates oscillations of period $2h$ and delocalizes the singularity. This is because in the discrete world, a Dirac is replaced by the function $D_n$ defined in (23) on a grid that coincides with the zeroes of $D_n$. When the grid is shifted and no longer coincides with these zeroes, we observe oscillations. The amplitude of the oscillations increases as the shift moves away from a gridpoint and this amplitude is maximal at the middle of two gridpoints (i.e., $\mathrm{mod}(s,h)=\frac{h}{2}$). There, the intensity of the peak drops by 36% and the peak is essentially spread over two pixels.

Now we have seen that slanting an image requires shifting each column with a shift that increases linearly with the column index. It is interesting to mention that if this rate of increase is rational $t=\frac{p}{q}$, then the shift is periodically exact every $q$ columns and spreads out transversally in-between (see Fig. 4, left). If $t$ is irrational, then the shifted column is never exact and oscillations 'spread' along the transverse direction.

Fig. 4 shows the effects of slanting images of ballistic parts computed by the forward solver, as we send a Dirac pulse or a Gaussian beam through the domain. Sending these inputs through the domain creates a line of variable width that will be rotated later on in order to compute the single scattering term. The Dirac case is seen on the left image, which shows oscillations that create ghost sources when the multiple scattering contributions to the transport solution are computed. Sending even quite narrow Gaussian beams instead of delta pulses suppresses most of the oscillations (see middle plot of Fig. 4). Despite the resulting slight loss in resolution, the information that travels across the domain is quite well localized, which al-

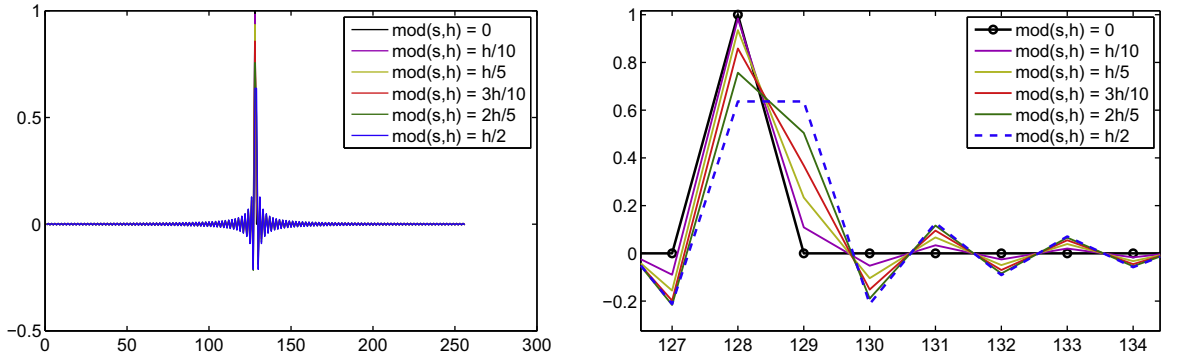


**Fig. 3.** Spectral numerical shifts of the Dirac function (right: close up). The amplitude of the oscillations is maximal when the singularity is shifted to the middle of two gridpoints.

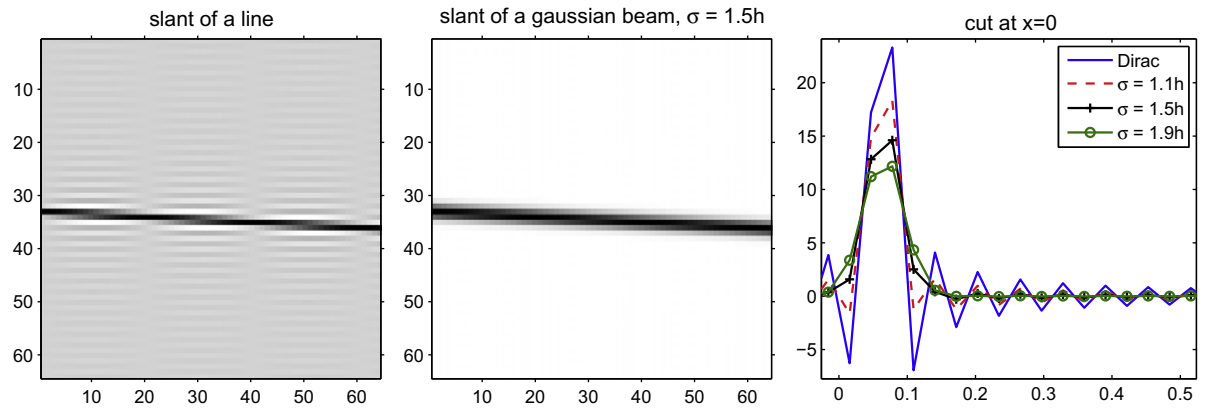


**Fig. 4.** Slanting a line with a rate $\frac{1}{10}$ $(\tan\theta = \frac{1}{10})$. Left: ray coming from a Dirac pulse, where we observe the periodicity of the transversal spreading pattern. Middle: Gaussian beam of width $1.5h$, where oscillations are essentially suppressed. Right: vertical cross section at '$x = 0$' of the slanted images of a Dirac pulse and a few Gaussian beams with variable width.

lows for an accurate computation of the singularities in the transport solution. As one can see from Fig. 4 (right), the beams become quite smooth when $\sigma \approx 1.5h$, which roughly corresponds to encoding a singularity over two-to-three grid points.

### 3.4.2. Effects of rotations

In the transport code, a rotation by $\theta$ requires a vertical slant with rate $\tan\theta$, followed by a horizontal slant with rate $\sin\theta$. For the uniform ordinate discretization we chose, these rates are usually irrational.

The rotation of a line typically first creates vertical oscillations after vertical slant. These vertical oscillations are then slanted horizontally, which creates new horizontal oscillations. The resulting image displays oscillations along two direc-

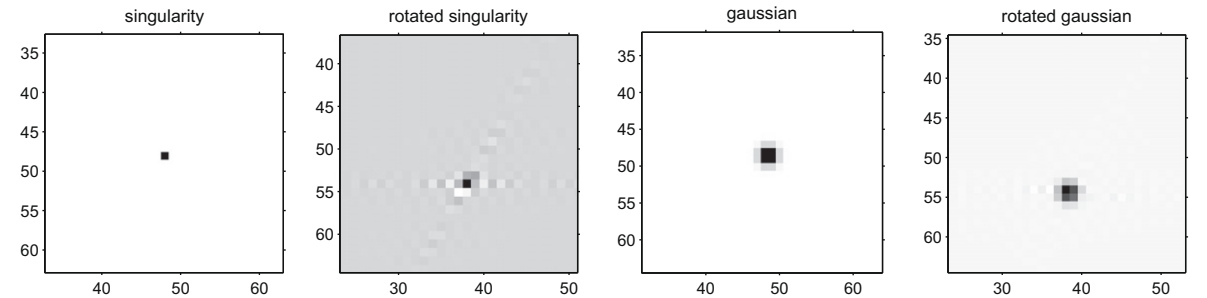


**Fig. 5.** Effects of rotations on singularities. Left: effect of a rotation $(\theta = \frac{\pi}{6})$ on a singular image. We observe oscillations along two directions and a peak of weaker intensity. Right: same with a narrow Gaussian spot of width $1.5h$, where $h$ is the spatial grid size. Oscillations almost disappear in that case.

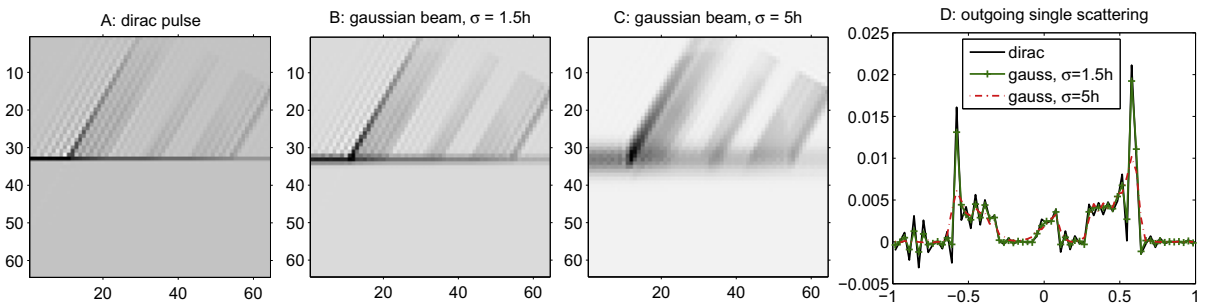


**Fig. 6.** Ballistic and single scattering contributions with different regularity of the incoming conditions. We send rays of increasing width on images (a), (b), (c), and look at the impact of the width on the re-emitted energy and the outgoing measurements (plots (d)) in direction $\frac{\pi}{3}$. The scattering map may be seen in Fig. 7, image (h). See text for more details.

tions (see Fig. 5, second from left). As we refine the grid, the amplitude of the oscillations does not change relative to the peak (this is the Gibb's effect) although their support decreases.

The rotation becomes much more accurate when the singularity is regularized. As we can see in Fig. 5 (second half), the oscillations disappear rather quickly as we approximate a point singularity with a narrow Gaussian spot. The finer the grid, the narrower is the Gaussian spot that prevents oscillations. Gaussian spots with width between 1 and 1.5 grid points, thus resulting in a loss of resolution comparable to 2–3 grid points, are sufficient to prevent spurious oscillations in practice.

Fig. 6 shows the effect of widening incoming Gaussian beams on the superposition of the ballistic part corresponding to the incoming direction $\theta_{\text{in}} = 0$ and single scattering propagating in direction $\theta_{\text{out}} = \frac{\pi}{3}$. Single scattering has been rescaled for better contrast. Images (a), (b) and (c) correspond to Gaussian beams with widths given by $0, 1.5h$, and $5h$, respectively (thus image (a) corresponds to a Dirac input). Wide Gaussian beams may be useful numerically, but can also be used to model sources with limited spatial resolution. Sub-plot (d) shows the outgoing measurements on $\Gamma_{+,\theta_{\text{out}}}$ for the previous three calculations. We observe that the wider the beam, the bigger is the support of the information that is re-emitted after scattering and thus the weaker is the resolution capabilities of the measured signals. At the same time, singular (Dirac) incoming conditions create singular sources in the single scattering calculations, which generates spurious oscillations as the singular source is rotated. Such oscillations are apparent on images (a) and (d).

## 4. Physical and controlled numerical blurring

### 4.1. Fokker Planck and Fermi pencil beam approximations

The numerical method presented above allows us to precisely capture the singularities of the albedo operator. In many practical settings, these singularities are substantially modified by some noisy physical effects. One such effect is the angular diffusion caused by peaked forward scattering. We refer the reader to [21] (see also [9]) for the derivation of Fokker Planck equations that model angular diffusion. We take here a slightly different route to obtain a model with angular diffusion. To simplify, we assume that $d = 2$ although the results (as in the rest of the paper) easily generalize to $d \geqslant 3$.

Let $v_i$ a discrete ordinate and $v_i^\perp$ its rotation by 90 degrees. Let $C_i \subset (0, 2\pi)$ the interval of measure $\delta$ centered at $\theta_i$. Then we have

$$v_i \cdot \nabla_x u + \sigma_i(x) u = \int_{(0,2\pi)\setminus C_i} k(x, \theta', \theta_i) u(t, x, \theta') d\theta' + \int_{C_i} k(x, \theta', \theta_i)(u(t, x, \theta') - u(t, x, \theta_i)) d\theta'. \tag{30}$$

Here, $\sigma_i(x) = \sigma(x) - \int_{C_i} k(x, \theta', \theta) d\theta'$, which we assume depends only on $x$. The first term on the right-hand side above is discretized as before. The second term, however, is approximated by a Taylor expansion

$$u(t, x, \theta') = u(t, x, \theta) + (\theta' - \theta)\partial_\theta u(t, x, \theta) + \frac{1}{2}(\theta' - \theta)^2 \partial_\theta^2 u(t, x, \theta) + l.o.t.$$

Assuming that $k(x, \theta', \theta_i)$ is symmetric in $\theta'$ about $\theta_i$, we find that $\int_{C_i} k(x, \theta', \theta_i)(\theta' - \theta_i) d\theta' = 0$. Thus, we observe that

$$\int_{C_i} k(x, \theta', \theta_i)(u(t, x, \theta') - u(t, x, \theta_i)) d\theta' = d(x)\partial_\theta^2 u(t, x, \theta_i) + l.o.t.,$$

where the effective angular diffusion coefficient is given by $d(x) = \int_{C_i} k(x, \theta', \theta_i) \frac{1}{2}(\theta' - \theta_i)^2 d\theta'$. When $k(\theta, \theta')$ is large for $\theta - \theta'$ close to 0, as it is the case for highly peaked forward scattering, the above coefficient $d(x)$ is non-negligible. Then (1) should be replaced, in all dimension $d \geqslant 2$, by

$$\begin{aligned} &v \cdot \nabla_x u + \sigma(x, v) u = d(x)\Delta_v u(x, v) + \int_{\mathbb{S}^{d-1}} k(x, v', v) u(x, v') dv', \quad \text{in } X \times \mathbb{S}^{d-1}, \\ &u(x, \theta) = g(x, \theta), \quad \text{on } \Gamma_-, \end{aligned} \tag{31}$$

where $\sigma$ and $k$ have been renormalized to account for the loss of the integral over $C_i$ in the scattering coefficient and where $\Delta_v$ represents the Laplace Beltrami operator on the sphere, which generalizes $\partial_\theta^2$ to arbitrary dimension $d \geqslant 2$.

In the setting of the source iteration method presented earlier, we thus want to solve problems of the form

$$\begin{aligned} &v \cdot \nabla_x u + \sigma(x) u = d(x)\Delta_v u(x, v) + f(x, v), \quad \text{in } X \times \mathbb{S}^{d-1}, \\ &u(x, v) = g(x, v), \quad \text{on } \Gamma_-. \end{aligned} \tag{32}$$

Here again, we assume that $\sigma = \sigma(x)$. The above equation generalizes (11).

When $d(x)$ is small, the above diffusion term does not significantly modify the direction of propagation. It is therefore possible to approximate the angular diffusion by a diffusion in the transverse angular variables only. When $d = 2$, this means a diffusion in the transverse variable $v(\theta)^\perp$ only. More precisely, let us assume that the main direction of propagation $v_0 = e_x$ (for instance after rotation in the numerical setting). When $d = 0$, the direction of propagation is fixed and equal to $\theta_0$. When

$d > 0$, angular diffusion causes $\theta$ to change. However, when $d$ is small, the angular diffusion remains small when the particles exit the domain on $\Gamma_+$. This allows us to formally replace the angle of propagation $(\cos\theta, \sin\theta)$ by $(1, \theta)$ as a first approximation. Then, the angular diffusion becomes the tangential diffusion $\partial_\theta^2$ so that a good approximation of (32) when $d(x)$ is small is the following Fermi pencil beam (FPB) approximation

$$\begin{aligned} &\frac{\partial u}{\partial \mathrm{x}} + \theta \frac{\partial u}{\partial \mathrm{y}} + \sigma(\mathrm{x},\mathrm{y})u = d(\mathrm{x},\mathrm{y})\frac{\partial^2 u}{\partial \theta^2} + f(\mathrm{x},\mathrm{y},\theta), \\ &u(0,\mathrm{y},\theta) = \delta(\mathrm{y})\delta(\theta). \end{aligned} \tag{33}$$

We recall that $x = (\mathrm{x}, \mathrm{y})$. The boundary conditions become initial conditions at x = 0, say. We are interested in singular incoming conditions so that y = 0 and $\theta = 0$ at x = 0. Because $d$ is small, variations in $\theta$ are small so that variations in $y$ are also small. As a result, $\sigma(\mathrm{x},\mathrm{y})$, $d(\mathrm{x},\mathrm{y})$ and $f(\mathrm{x},\mathrm{y},\theta)$ may be replaced, up to an order of accuracy comparable to the difference between the solutions (32) and (33), by $\sigma(\mathrm{x},0)$, $d(\mathrm{x},0)$ and $f(\mathrm{x},0,\theta)$. We are thus interested in the evolution equation (in the x variable)

$$\begin{aligned} &\frac{\partial u}{\partial \mathrm{x}} + \theta \frac{\partial u}{\partial \mathrm{y}} + \sigma(\mathrm{x})u = d(\mathrm{x})\frac{\partial^2 u}{\partial \theta^2} + f(\mathrm{x},\theta), \\ &u(0,\mathrm{y},\theta) = \delta(\mathrm{y})\delta(\theta), \end{aligned} \tag{34}$$

where the dependence of $\sigma, d$, and $f$ in y has been neglected.

When $f = 0$, the above equation admits an explicit expression:

$$\begin{aligned} &u(\mathrm{x},\mathrm{y},\theta) = e^{-\int_0^{\mathrm{x}} \sigma(t)\,dt} \frac{1}{2\pi\sqrt{C(\mathrm{x})}} \exp\left(-\frac{1}{C(\mathrm{x})}\left[D_0(\mathrm{x})(\mathrm{y}-\mathrm{x}\theta)^2 + 2D_1(\mathrm{x})(\mathrm{y}-\theta\mathrm{x})\theta + D_2(\mathrm{x})\theta^2\right]\right), \\ &\text{where} \quad D_i(\mathrm{x}) = \int_0^{\mathrm{x}} t^i d(t)\,dt, \quad i = 0,1,2, \qquad C(\mathrm{x}) = D_0(\mathrm{x})D_2(\mathrm{x}) - D_1^2(\mathrm{x}). \end{aligned} \tag{35}$$

This explicit expression allows us to replace the angular diffusion coupled with the spatial drift by a spatial diffusion in the y variable with a x-dependent diffusion coefficient. Averaging over the angular variable in (35), we obtain after some algebra that

$$U(\mathrm{x},\mathrm{y}) := \int_{\mathbb{R}} u(\mathrm{x},\mathrm{y},\theta)\,d\theta = e^{-\int_0^{\mathrm{x}} \sigma(t)\,dt} \frac{1}{w(\mathrm{x})\sqrt{2\pi}} e^{-\frac{\mathrm{y}^2}{2w^2(\mathrm{x})}}, \tag{36}$$

where $w^2(\mathrm{x}) = 2\left(D_2(\mathrm{x}) - 2\mathrm{x}D_1(\mathrm{x}) + \mathrm{x}^2 D_0(\mathrm{x})\right)$. Then we can show that $U(\mathrm{x},\mathrm{y})$ satisfies the parabolic equation

$$\begin{aligned} &\frac{\partial U}{\partial \mathrm{x}} + \sigma(\mathrm{x})U = d_{\mathrm{FPB}}(\mathrm{x})\frac{\partial^2 U}{\partial \mathrm{y}^2}, \\ &U(0,\mathrm{y}) = \delta(\mathrm{y}), \end{aligned} \tag{37}$$

where the diffusion coefficient has the following expression

$$d_{\mathrm{FPB}}(\mathrm{x}) = \frac{d}{d\mathrm{x}}\left(\frac{w(\mathrm{x})^2}{2}\right) = 2\int_0^{\mathrm{x}} (\mathrm{x}-t)d(t)\,dt. \tag{38}$$

Eq. (37) is the equation we solve numerically. This equation allows us to incorporate the physical effect caused by small angular diffusion. Note that when $d(t) = d$ is constant, then $w(\mathrm{x})$ is proportional to $x^{\frac{3}{2}}$. This shows that $U(\mathrm{x},\mathrm{y})$ is then a function of $\frac{y}{x^{\frac{3}{2}}}$. Diffusion in the FPB model increases super-linearly in the x variable.

### 4.2. Blurred ballistic and single scattering components

We now consider the effect of blurring by angular diffusion on the transport solutions. We consider two types of blurring, the Fermi pencil beam (FPB) blurring presented in the preceding section and the linear diffusion (LD) blurring, which is also of the form (37) though with a different form for the diffusion coefficient than (38). The latter diffusion will be described in detail in the next section. Our numerical results correspond as in Fig. 6 to an incoming direction $\theta_{\mathrm{in}} = 0$ and single scattering propagating in direction $\theta_{\mathrm{out}} = \frac{\pi}{3}$.

The numerical results are gathered in Fig. 7. Images (a), (b) and (c) show the ballistic parts passing through the domain in the case of no blurring (a), FPB blurring (b), and LD blurring (c). The scattering map given in Image (h) is also represented in the background of Images (a)–(c). The source term $Ku_0(x)$ generated as in (12) for the construction of the single scattering contribution is presented in images (e), (f), and (g) after rotation by an angle $\frac{\pi}{3}$ for the three cases of images (a), (b), and (c), respectively. Note that single scattering is much more diffuse in the presence of angular or linear diffusion away from the location of the incoming source term (point with coordinates (33,1) in images (a)–(c) and coordinates about (22,14) in images (e), (f), and (g) after rotation). Close to that location, the single scattering term displays some oscillations caused by the rotation as for the results presented in Fig. 6. The superposition of the ballistic and single scattering (rescaled for bet-

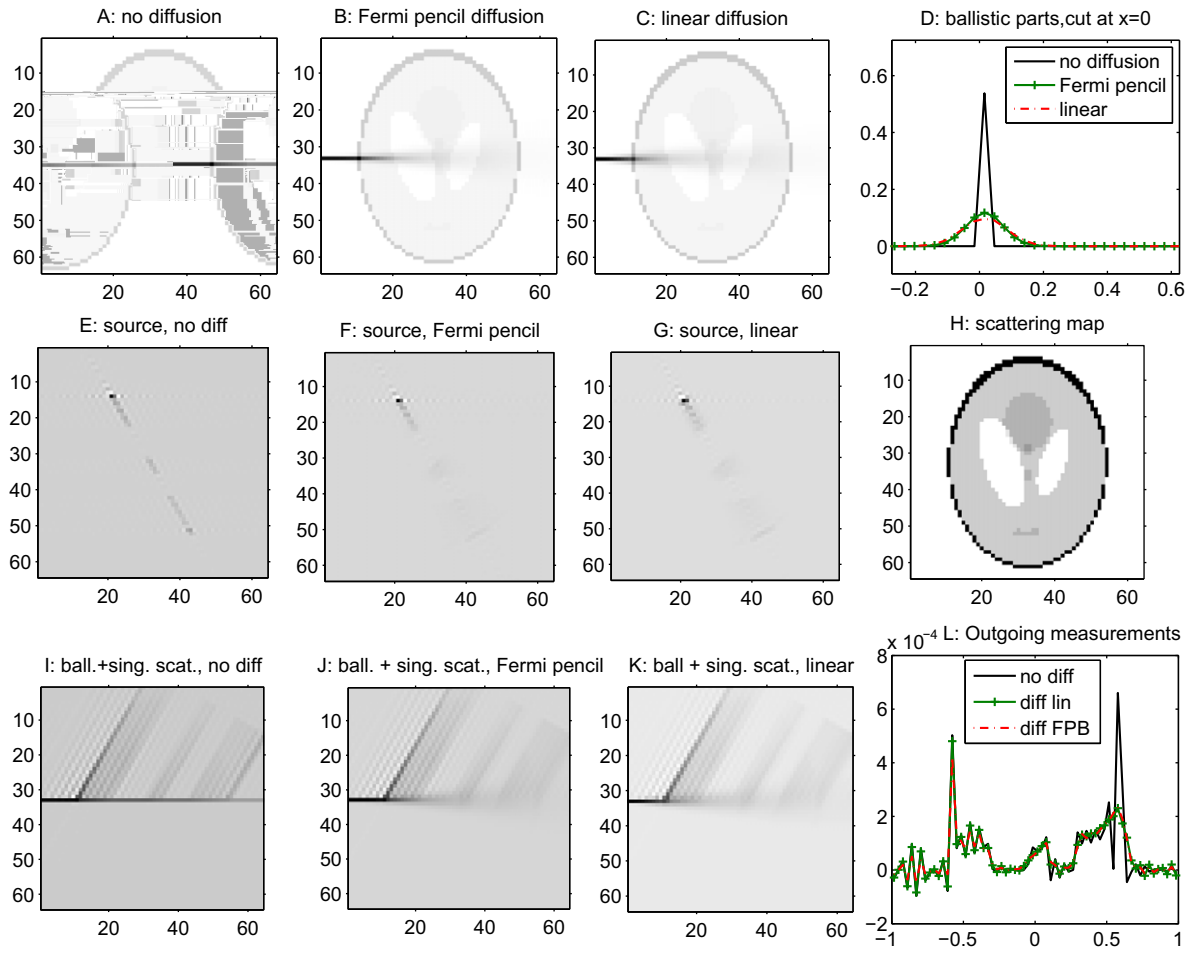


**Fig. 7.** Different types of diffusion and their effects on ballistic parts and single scattering; see text for details. The linear diffusion leads to a linear widening, whereas the Fermi pencil diffusion with constant diffusion coefficient leads to a geometric widening of rate $\frac{3}{2}$.

ter contrast) in the three scenarios is presented in Images (i), (j), and (k), respectively. Unlike the situation encountered in Fig. 6, the ballistic and single scattering terms are seen to become smoother as the distance to the location of the incoming source term increases. Such smoothing is very damaging for the inverse problem since the blurred small scale structures are essentially lost in the measurements. A cross section of the single scattering measurements on top of the domain $\Omega$ is shown in Image (l).

### 4.3. Blurring and ray effects

As we mentioned in the introduction, one of the drawbacks of the discrete ordinates method is the so-called ray effect; see Fig. 8. Angular diffusion, giving rise to spatial diffusion, may ray effect. With a diffusion coefficient that depends on the distance to the localized source term, we can construct a solution that is very close to the exact ballistic part.

The diffusion coefficient is derived so that the spatial density of the ballistic part best approximates that of the solution of the continuous problem. Let us consider the free transport equation in $X$ with a point source at 0 and zero incoming boundary condition:

$$v \cdot \nabla_x u = \delta(x)\varphi(\theta), \quad x \in X,\ \theta \in \mathbb{S}^1; \quad u|_{\Gamma_-} = 0. \tag{39}$$

Then the spatial density $U$ of the solution $u$ is given by:

$$U(x) = \int_{S^1} u(x,\theta)\,d\theta = \frac{1}{|x|}\varphi(\theta). \tag{40}$$

This has to be compared with the spatial density of the solution, which solves the same problem in discrete ordinates,

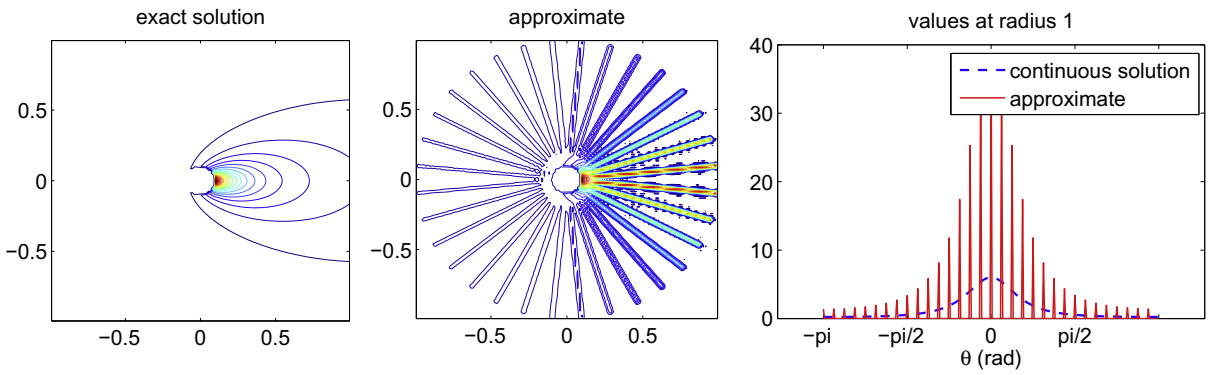


**Fig. 8.** Illustration of the ray effect. The spatial density of the discrete ordinates solution (middle) is supported along rays emanating from the source point. Right: values of exact and approximate angular densities on a circle centered at the point source. The function $\varphi$ is defined in (43). The singularities at $x = 0$ are removed from the pictures to increase contrast.

$$v_i \cdot \nabla_x u = \delta(x)\varphi(\theta_i), \quad x \in X,\ i = 1, \ldots, N_d; \quad u|_{\Gamma_-} = 0. \tag{41}$$

The approximate spatial density is supported on $N_d$ rays emanating from the point source position and has the expression

$$\widetilde{U}(x) = \sum_{i=1}^{N_d} \varphi(\theta_i)\delta\left(\theta_i - \frac{x}{|x|}\right), \quad x \neq 0. \tag{42}$$

See Fig. 8, where we used the phase function

$$\varphi(\theta) = \frac{1 - g^2}{(1 + g^2 - 2g\cos\theta)^{\frac{3}{2}}}, \quad \text{with } g = 0.5, \tag{43}$$

which is referred to as the Henyey–Greenstein phase function with anisotropy coefficient $g = 0.5$.

This effect induced by the angular discretization is called the ray effect, and in order to reduce it, we need to spread the rays over the gaps between discrete rays. Since each ray is computed by solving an ODE along the direction of the ray, we can use diffusion to spread each ray transversally. Looking at the spatial densities on concentric circles centered at 0 with increasing radii, the graph of $\varphi(\theta)$ is stretched linearly and decreases like $\frac{1}{|x|}$ whereas the discretized solution is a Dirac comb. By adding transverse diffusion, we approximately convolve this Dirac comb with a Gaussian function (the Green's function for the diffusion equation). When the variance of the Gaussian function is chosen appropriately and $\varphi$ is a smooth function, then the numerical density is quite close to the exact solution. On a circle of radius $R$, the comb's step-size is $R\sigma,\ \sigma = \frac{2\pi}{N_d}$. Then, for each direction $\theta_i$, we replace a delta pulse by a normalized Gaussian beam, the width of which increases linearly with the distance to the source point. For a direction $\theta_i$, we want the expression

$$u(x, \theta_i) = \frac{\varphi(\theta_i)}{\sigma\sqrt{2\pi}|x \cdot v_i|} \exp\left(-\frac{(x \cdot v_i^{\perp})^2}{2\sigma^2(x \cdot v_i)^2}\right), \quad x \cdot v_i > 0. \tag{44}$$

This function can be generated by solving the parabolic equation (on the half-domain $X \cap \{x \cdot v_i > 0\}$)

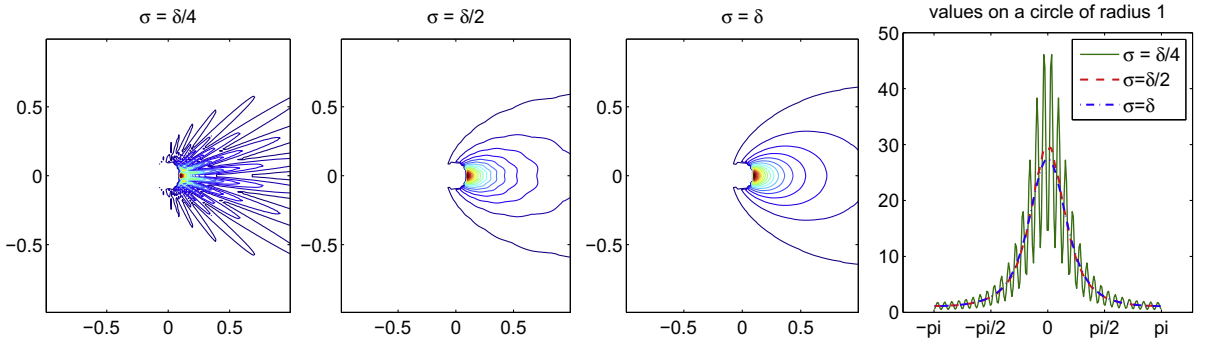


**Fig. 9.** We address the ray effect by spreading the beams transversally. Compare with the results in Fig. 8 (left) where the same phase function is used. When the spreading is too small, the gaps between the rays are not filled (left). As the constant $\sigma$ becomes close to $\delta$ (middle two), we recover the shape of the continuous density. Right: values of the three solutions on a disk of radius 1 centered at 0. The singularities at $x = 0$ are removed to increase contrast.

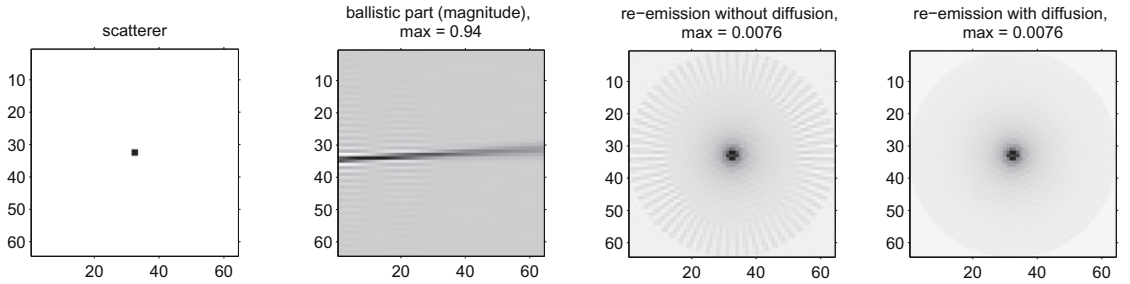


**Fig. 10.** Effects of blurring on single scattering.

$$\begin{aligned} &v_i \cdot \nabla_x u = \sigma^2 (x \cdot v_i)\left(v_i^{\perp} \cdot \nabla_x\right)^2 f, \quad x \cdot v_i > 0, \\ &u|_{\{x \cdot v_i = 0\}} = \varphi(\theta_i)\delta_0. \end{aligned} \tag{45}$$

Fig. 9 shows the numerical superposition of these beams for a few values of $\sigma$.

We have implemented the simulation of the diffusion terms in (37) and (45) by modifying the ODE method described in Section 3.3 and replacing it by the solution of standard parabolic equations. Our implementation is a standard Euler explicit method (second-order in the spatial variable y, first-order in the "time" variable x). In the variables of the rotating frame, this amounts to adding the three-point discretization of the term $d(\mathrm{x})\frac{\partial^2 u}{\partial y^2}$ in (29). We verify that the CFL condition for such a scheme is

$$d(\mathrm{x}) \leqslant \frac{\Delta \mathrm{y}^2}{2\Delta \mathrm{x}}. \tag{46}$$

In this paper, we are interested in small diffusion coefficients acting as uncontrolled noise. In our simulations, the diffusion coefficient $d$ was always chosen sufficiently small that the above CFL condition would be satisfied with $\Delta \mathrm{y} = \Delta \mathrm{x}$. In the diffusion model (45) that addresses the ray effect, we find that $d = \left(\frac{2\pi}{N_d}\right)^2 L$, where $L$ is the distance to the source, and for diffusion coming from the Fermi-Pencil-Beam approximation (37), we obtain that $d = CL^2$, where $C$ is a constant that depends on the peak-forwardness of the scattering coefficient. In cases where the diffusion coefficient is larger than $\Delta \mathrm{x}/2$, we then need to chose a finer discretization in the direction x that restores (46) or solve the PDE by implicit methods at the cost of an obvious loss in resolution.

As an implementation in the forward solver, Fig. 10 shows a small scatterer being hit by a beam with or without transverse diffusion, as well as the single scattering part that is re-emitted from it. The mid-left picture shows the ballistic part, whereas the mid-right and rightmost pictures show single scattering without and with blurring. The input beam loses energy as it hits the scatterer at the center of the image, and this energy is redistributed through space in the two pictures on the right. We can observe a clear manifestation of the ray effect in the re-emission images, where the single scattering is present everywhere in the domain in the presence of blurring, and is concentrated along rays otherwise. It should be noted that the diffusion coefficient depends on the source location. The numerical tool to address ray effects therefore becomes much less tractable when the source is not supported on a small number of points in the domain or at its boundary.

We conclude that in order to detect a localized scatterer, it is crucial to add transverse diffusion to the forward solver since otherwise, any object located in one of these non-emission areas (see Fig. 10, mid-right) would not receive any energy from the first scatterer. The solution we propose is not very practical since the diffusion depends on the scatterer position, and this information may not be known in practice. A method that would be independent of the source position consists of implementing angular (rather than spatial) diffusion. Such diffusion would be significantly more costly numerically and is not considered here.

## 5. Inverse transport reconstructions

This section addresses the numerical simulation of the inverse transport problem presented in Section 2.2 using the method described in Section 3. The albedo operator (7) involves the solution of forward transport equations and is thus discretized using the numerical method of Section 3. The inverse problem consists of reconstructing the discretized optical coefficients from the discretized albedo operator.

The reconstruction of optical parameters from boundary measurements has been considered in many settings and regimes of transport; see e.g. [4,14,29]. Most techniques are based on optimization procedure that minimize the error between predicted and available measurements. Rather, we base here our inversion algorithm on the singular decomposition (7) and the explicit formulas (9) and (10). A similar strategy was considered in [3]. The first formula allows us to estimate line integrals of the total attenuation coefficient $\sigma$. The reconstruction of $\sigma$ from its line integrals requires that we apply an inverse Radon transform. Our practical choice for the discrete inverse Radon transform is a standard filtered back-projection function

`iradon` as it is implemented in MatLab. The second formula (10) is then used to solve for the scattering coefficient by a point-wise estimate. The inverse transport simulation is thus directly related to the exact, continuous, decomposition of the albedo operator. It is therefore crucial that these terms be calculated accurately, which is done by the numerical tool presented in the preceding sections.

In preparation for the numerical inversion, we recall the definition of the Radon Transform. For $r \in \mathbb{R}$ and $\theta \in (0, 2\pi)$, the line of coordinates $(r, \theta)$, is defined as the set

$$L(r,\theta) := \{ r v^\perp + t v,\ t \in \mathbb{R} \}, \quad v = (\cos\theta, \sin\theta). \tag{47}$$

For a sufficiently smooth function $f$ defined in $\mathbb{R}^2$, we define its Radon Transform $\mathcal{R}f$ on $\mathbb{R} \times (0, 2\pi)$ as

$$\mathcal{R}f(r,\theta) := \int_{L(r,\theta)} f = \int_{\mathbb{R}} f(r v^\perp + t v)\, dt, \quad r \in \mathbb{R},\ \theta \in (0, 2\pi). \tag{48}$$

Note that the lines $L(r,\theta)$ and $L(-r,-\theta)$ are equal so that $\mathcal{R}f(r,\theta) = \mathcal{R}f(-r,-\theta)$ for $(r,\theta) \in \mathbb{R} \times (0,2\pi)$.

### 5.1. Singular decomposition of the discrete albedo operator

In the rest of the section, we consider inverse transport problems of the following type. We assume that the scattering coefficient $k = k(x)$ is independent of $\theta$ and $\theta'$ and is smooth. The intrinsic attenuation coefficient $\sigma_a(x)$ is allowed to be singular (i.e., have jump discontinuities). This setting is adapted e.g. to optical tomography, where the scattering coefficient is typically relatively smooth and the absorption coefficient provides a large contrast between healthy and un-healthy tissues. Note that the total absorption $\sigma(x) = \sigma_a(x) + \sigma_p(x)$ with $\sigma_p(x) = 2\pi k(x)$ is thus also possibly singular.

The ballistic part is calculated with some blurring corresponding to angular diffusion. We recall that the angular diffusion model developed in Section 4 requires that we know the (localized) source location. For smooth, delocalized, scattering coefficients, blurring is not very important and would be very expensive to compute. The single and multiple scattering components are therefore treated without any blurring.

The measurements are therefore modeled as follows. Following the geometry described in Fig. 1, the set of incoming conditions is parameterized by $r \in [-1,1]$ for each $\theta \in (0, 2\pi)$. The ballistic term is also parameterized by $\theta \in (0, 2\pi)$ and $r \in [-1,1]$ on $\Gamma_{+,\theta}$. More precisely, let $g$ be a singular incoming boundary condition supported at position $r_{\text{in}} \in [-1,1]$ and of intensity $I_{\text{in}}$. Then in the presence of blurring caused by angular diffusion, $\mathcal{A}_0 g$ is supported on $\Gamma_{+,\theta_{\text{in}}}$ and in the Fermi pencil beam approximation, is given by

$$\mathcal{A}_0 g(r,\theta_{\text{in}}) = \frac{I_{\text{in}}}{\sigma_d \sqrt{2\pi}} e^{-\frac{(r-r_{\text{in}})^2}{2\sigma_d^2}} e^{-\mathcal{R}\sigma(r_{\text{in}},\theta_{\text{in}})}, \quad r \in [-1,1], \tag{49}$$

where the width $\sigma_d$ is related to the diffusion coefficient by the relation $\sigma_d^2 = 2\mathcal{R} d_{\text{FPB}}(r_{\text{in}}, \theta_{\text{in}})$.

As we mentioned already, the scattering terms are calculated numerically in the absence of any numerical blurring. Though the source generated by the ballistic contribution indeed was blurred, it is still concentrated in the vicinity of the line of support of the exact ballistic part. Under these hypotheses, the single scattering contribution is then approximately given by

$$\mathcal{A}_1 g(r_{\text{out}}, \theta_{\text{out}}) = \frac{I_{\text{in}}}{\sin(\theta_{\text{out}} - \theta_{\text{in}})} k(x, \theta_{\text{in}}, \theta_{\text{out}}) E_\sigma(x_{\text{in}}, x, x_{\text{out}}), \tag{50}$$

where $x = (\mathrm{x}, \mathrm{y})$ is the intersection of the lines $L(r_{\text{in}}, \theta_{\text{in}})$ and $L(r_{\text{out}}, \theta_{\text{out}})$ given by

$$\begin{bmatrix} \mathrm{x} \\ \mathrm{y} \end{bmatrix} = \frac{1}{\sin(\theta_{\text{out}} - \theta_{\text{in}})} \begin{bmatrix} \cos\theta_{\text{out}} & -\cos\theta_{\text{in}} \\ \sin\theta_{\text{out}} & -\sin\theta_{\text{in}} \end{bmatrix} \cdot \begin{bmatrix} r_{\text{in}} \\ r_{\text{out}} \end{bmatrix},$$

and $E_\sigma(x_{\text{in}}, x, x_{\text{out}})$ encodes the exponential terms in (10) that account for the total attenuation along the broken line $[x_{\text{in}}, x, x_{\text{out}}]$. It remains to choose $\theta_{\text{in}}$ and $\theta_{\text{out}}$ among the set of discrete ordinates $\Theta_\delta$ and $r_{\text{in}}$ and $r_{\text{out}}$ as one of the spatial grid points to obtain a discretization of the ballistic and single scattering contributions of the measurements.

Let us for the moment assume that $\mathcal{A}_0$ and $\mathcal{A}_1$ have been measured. Then the reconstruction of the optical coefficients is performed as follows.

(i) From knowledge of $\mathcal{A}_0$, we extract the term $\mathcal{R}\sigma(r_{\text{in}}, \theta_{\text{in}})$ for all $(r_{\text{in}}, \theta_{\text{in}})$ in the discretized spaces for $[-1,1] \times (0, 2\pi)$. We then apply the inverse Radon transform (MatLab's function `iradon`) to the data to reconstruct the total attenuation $\sigma(x)$.

(ii) From knowledge of $\mathcal{A}_1$ and of $\sigma(x)$ reconstructed in the preceding step, we reconstruct $k(x, \theta_{\text{in}}, \theta_{\text{out}}) := k(x)$ on the Cartesian grid.

Since $k(x)$ is independent of the directions $\theta_{\text{in}}, \theta_{\text{out}}$, we can choose them freely. We consider here the case $\theta_{\text{in}} = 0$. We will present reconstructions based on several values of $\theta_{\text{out}}$, which show how the images degrade as $\theta_{\text{out}}$ converges to $\theta_{\text{in}}$. The attenuation coefficient $E_\sigma$ needs to be estimated carefully. Several methods for doing so are described below.

The next two paragraphs show how the total attenuation and scattering coefficients may be reconstructed from knowledge of $\mathcal{A}_0$ and $\mathcal{A}_1$. The available measurements, however, consist of the full albedo operator $\mathcal{A} := \mathcal{A}(r_{\text{in}}, \theta_{\text{in}}; r_{\text{out}}, \theta_{\text{out}})$, the value of the measurements taken at coordinates $(r_{\text{out}}, \theta_{\text{out}}) \in \Gamma_{+,\theta_{\text{out}}}$ when sending a (delta or Gaussian) beam centered at $(r_{\text{in}}, \theta_{\text{in}}) \in \Gamma_{-,\theta_{\text{in}}}$.

Since measurements $\mathcal{A}$ are well approximated by $\mathcal{A}_0$ when $\theta_{\text{in}} = \theta_{\text{out}}$ and by $\mathcal{A}_1$ when $\theta_{\text{in}} \neq \theta_{\text{out}}$, we may replace $\mathcal{A}_0$ and $\mathcal{A}_1$ above by the available measurements $\mathcal{A}$ and obtain a first reconstruction of the optical parameters. Once the parameters are estimated, the transport solution (1) can be solved to estimate $\mathcal{A} - \mathcal{A}_0$ and $\mathcal{A} - \mathcal{A}_1$. Such residuals can then be removed from the measured operator $\mathcal{A}$ to obtain better approximations for $\mathcal{A}_0$ and $\mathcal{A}_1$. These new approximations may then be used to estimate the optical parameters more accurately, which in turn improve the estimate of the terms $\mathcal{A} - \mathcal{A}_0$ and $\mathcal{A} - \mathcal{A}_1$. This generates an iterative algorithm that converges to the "true" optical parameters, at least in the absence of noise, provided that the initial step offers a sufficiently accurate description of the optical parameters; see also [30] for a theoretical justification of the algorithm in dimension $d = 2$. The iterative algorithm is described in Section 5.4 after we present the initial step, which consists of reconstructing the optical parameters from knowledge of $\mathcal{A}_0$ and $\mathcal{A}_1$.

### 5.2. Reconstruction of the total attenuation map

This section considers the reconstruction of $\sigma(x)$ from knowledge of $\mathcal{A}_0$. For every discrete radius $r_i$ and ordinate $\theta_j$, we propagate a Dirac pulse of intensity $I_{\text{in}}$ through the domain $X$ starting from position $(r_i, \theta_j)$ and collect the ballistic measurements on $\Gamma_{+,\theta_j}$ after solving a forward transport problem.

#### 5.2.1. Reconstructions without blurring

In the absence of noise, we have

$$\mathcal{A}_0(r_i, \theta_j; r_i, \theta_j) = I_{\text{in}} e^{-\mathcal{R}\sigma(r_i,\theta_j)},$$

and the Radon transform of $\sigma(x)$ is obtained as

$$\mathcal{R}\sigma(r_i, \theta_j) = -\log\left(\frac{\mathcal{A}_0(r_i, \theta_j; r_i, \theta_j)}{I_{\text{in}}}\right). \tag{51}$$

The total attenuation coefficient is then reconstructed by application of an inverse Radon transform. Figs. 11 and 12 show reconstructions for a smooth map and a discontinuous map, respectively. In each case, we have $128 \times 128$-size images with 128 discrete ordinates.

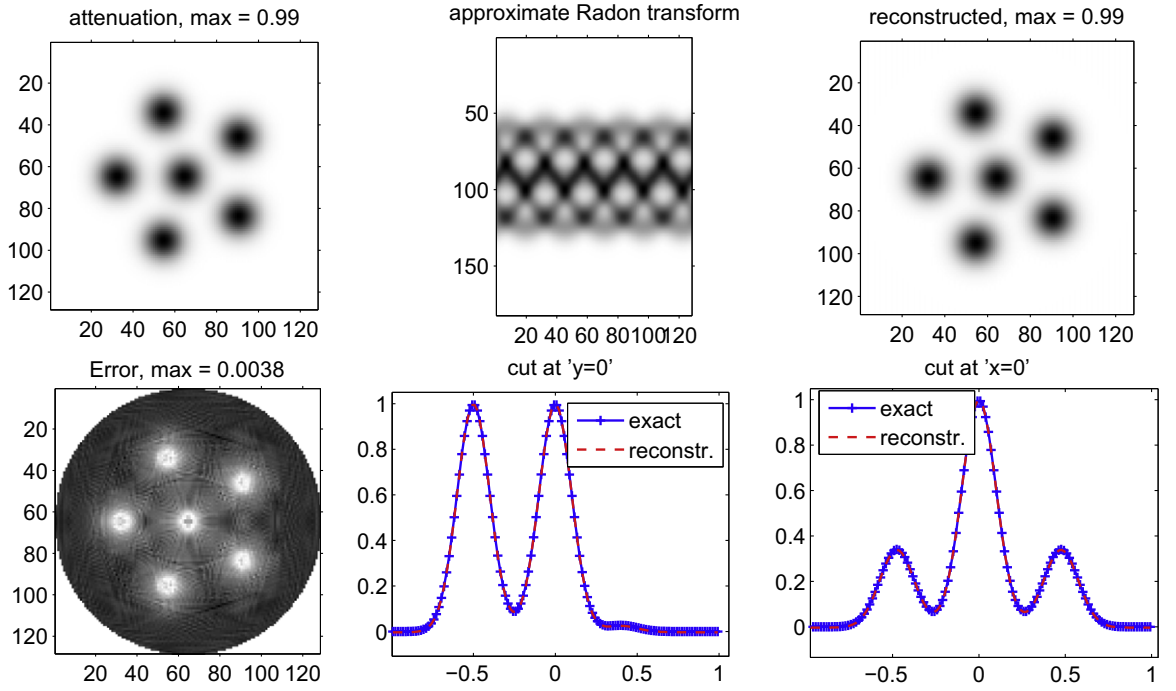


**Fig. 11.** Reconstruction of a smooth attenuation map. The relative (discrete) $L^2$ error is approximately 1.1%.

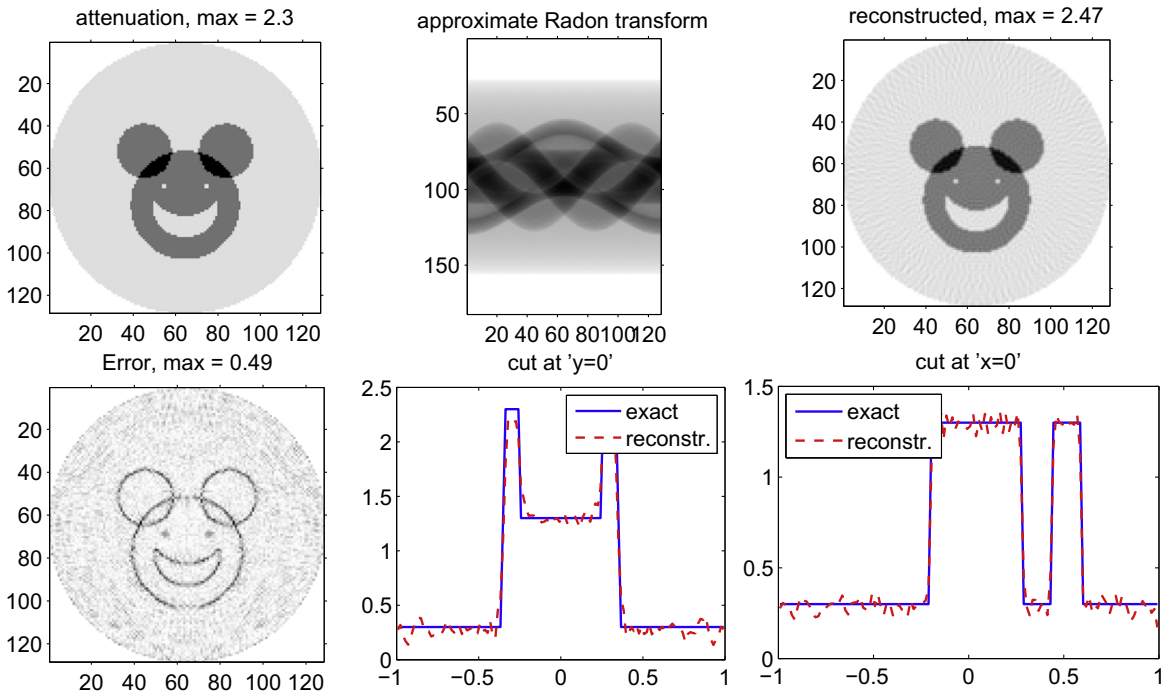


**Fig. 12.** Reconstruction of a discontinuous attenuation map. The relative (discrete) $L^2$ error is on the order of 10%. Most of the error is supported in the vicinity of the discontinuities.

*5.2.2. Reconstructions with blurring*

In the presence of blurring caused by angular diffusion as modeled in Section 4.1, the ballistic measurements are given by

$$\mathcal{A}_0(r_i,\theta_j;r,\theta_j) \approx \frac{I_{\text{in}}}{\sigma_d\sqrt{2\pi}} e^{-\frac{(r-r_i)^2}{2\sigma_d^2}} e^{-\mathcal{R}\sigma(r_i,\theta_j)}, \quad r\in[-1,1], \tag{52}$$

where $\sigma_d \ll 1$ is the width of the Gaussian blurring. Several methods can then be devised to extract $\mathcal{R}\sigma(r_i,\theta_j)$ from such a term. We propose four similar formulas. The first two formulas are independent of the spatial discretization and are given by

$$\mathcal{R}\sigma(r_i,\theta_j) = -\log\left(\frac{\sigma_d\sqrt{2\pi}\mathcal{A}_0(r_i,\theta_j;r_i,\theta_j)}{I_{\text{in}}}\right), \quad \text{(ratio of the peaks)}, \tag{53}$$

$$\mathcal{R}\sigma(r_i,\theta_j) = -\log\left(\frac{\int_{-1}^{1}\mathcal{A}_0(r_i,\theta_j;r,\theta_j)\,dr}{I_{\text{in}}}\right), \quad \text{(ratio of the energies)}. \tag{54}$$

Formula (53) measures the outgoing density at the peak of the Gaussian blurring caused by angular diffusion. It requires prior knowledge of the smoothing coefficient $\sigma_d$. Formula (54) is based on the fact that the angular diffusion preserves particles. When $[-1,1]$ is replaced by $\mathbb{R}$, the above formula is exact at the continuous level. Note that it does not require prior knowledge of $\sigma_d$ and is therefore the only choice in a situation where the blurring caused by angular diffusion is not known. In our simulations, reconstructions based on (54) appeared to be more robust than the ones based on (53). This is because when blurring is small, rays that are sent close to the edges of the interval $[-1,1]$ do not sufficiently diffuse to resemble Gaussian functions when they exit the domain. Formula (53) is then inaccurate. Formula (54) is not affected by such an effect. Even when the diffusion scheme is not very accurate, it still preserves the number of particles. This artifact can be lessened by having the support of the optical coefficients strictly smaller than the computational domain so that the quantities of interest are not significantly affected by this artifact.

In practice, we also expect (54) to be more useful as it does not assume any specific structure for the blurring function and does not require exact knowledge of the exiting point $r_i$ as (53) does. Both formulas assume that the angular diffusion is accurately captured by the numerical scheme, which implies that $\sigma_d$ is large compared to the spatial grid size. This constraint is very difficult to meet in practice.

Two similar formulas are useful when the spatial discretization occurs at the same scale as the angular diffusion, for instance when the variance $\sigma_d$ corresponds to a few grid points. Then the blurring caused by the noise is not well approxi-

mated by the continuous formula (52). To account for the numerical artifacts, we can calculate the blurring that would occur in the absence of absorption, i.e., calculate $\mathcal{A}_{0,d} := \mathcal{A}_0$ with $\sigma \equiv 0$, and calibrate the albedo operator accordingly. This yields the formulas

$$\mathcal{R}\sigma(r_i,\theta_j) = -\log\left(\frac{\mathcal{A}_0(r_i,\theta_j;r_i,\theta_j)}{\mathcal{A}_{0,d}(r_i,\theta_j;r_i,\theta_j)}\right), \quad \text{(ratio of the peaks)}, \tag{55}$$

$$\mathcal{R}\sigma(r_i,\theta_j) = -\log\left(\frac{\int_{-1}^{1}\mathcal{A}_0(r_i,\theta_j;r,\theta_j)\,dr}{\int_{-1}^{1}\mathcal{A}_{0,d}(r_i,\theta_j;r,\theta_j)\,dr}\right), \quad \text{(ratio of the energies)}. \tag{56}$$

Such formulas require that the angular diffusion coefficient be known in order to calculate $\mathcal{A}_{0,d}$. They are useful in the sense that the ratios $\frac{\mathcal{A}_0(r_i,\theta_j;r_i,\theta_j)}{\mathcal{A}_{0,d}(r_i,\theta_j;r_i,\theta_j)}$ depend very little on the discretization used in the numerical simulation. As such, they provide a good tool to understand the effect of given, known, angular diffusion on the physical measurements used in the reconstructions. Which formula is best thus depends on the practical situation of interest. The numerical tool developed in Section 3 allows for sufficient flexibility to handle several practically relevant noise models in the ballistic measurements. A numerical application of the formulas involving blurring is presented in Fig. 13.

### 5.3. Reconstruction of the scattering coefficient

We now address the reconstruction of $k(x,\theta',\theta)$ from knowledge of $\mathcal{A}_1$ and $\sigma(x)$. This requires that we estimate $E_\sigma(x_{\text{in}},x,x_{\text{out}})$ accurately. Assume that $\theta_{\text{in}}$ and $\theta_{\text{out}}$ are fixed and define $\alpha = \theta_{\text{out}} - \theta_{\text{in}}$. Let also

$$r_i = -1 + \frac{2i-1}{n}, \quad 1 \leqslant i \leqslant n. \tag{57}$$

We run $n$ forward solvers with incoming boundary conditions on $\Gamma_{-,\theta_{\text{in}}}$ located at $x_i^- := -v_{\text{in}} + r_i v_{\text{in}}^\perp$ for $i = 1,\dots,n$ (we recall that $v_{\text{in}} = (\cos\theta_{\text{in}}, \sin\theta_{\text{in}})$ and $v_{\text{out}}$ is defined equivalently). We then reconstruct $k(\cdot,\theta_{\text{in}},\theta_{\text{out}})$ at the points $\{x_{ij}\}_{j=1}^n$ defined by

$$x_{ij} = -r_j v_{\text{in}} + r_i v_{\text{in}}^\perp, \quad 1 \leqslant j \leqslant n.$$

These points project on to the boundary $\Gamma_{+,\theta_{\text{out}}}$ at the points

$$x_{ij}^+ := v_{\text{out}} + r_{ij} v_{\text{out}}^\perp, \quad \text{where } r_{ij} := -r_j \sin\alpha + r_i \cos\alpha, \quad 1 \leqslant j \leqslant n.$$

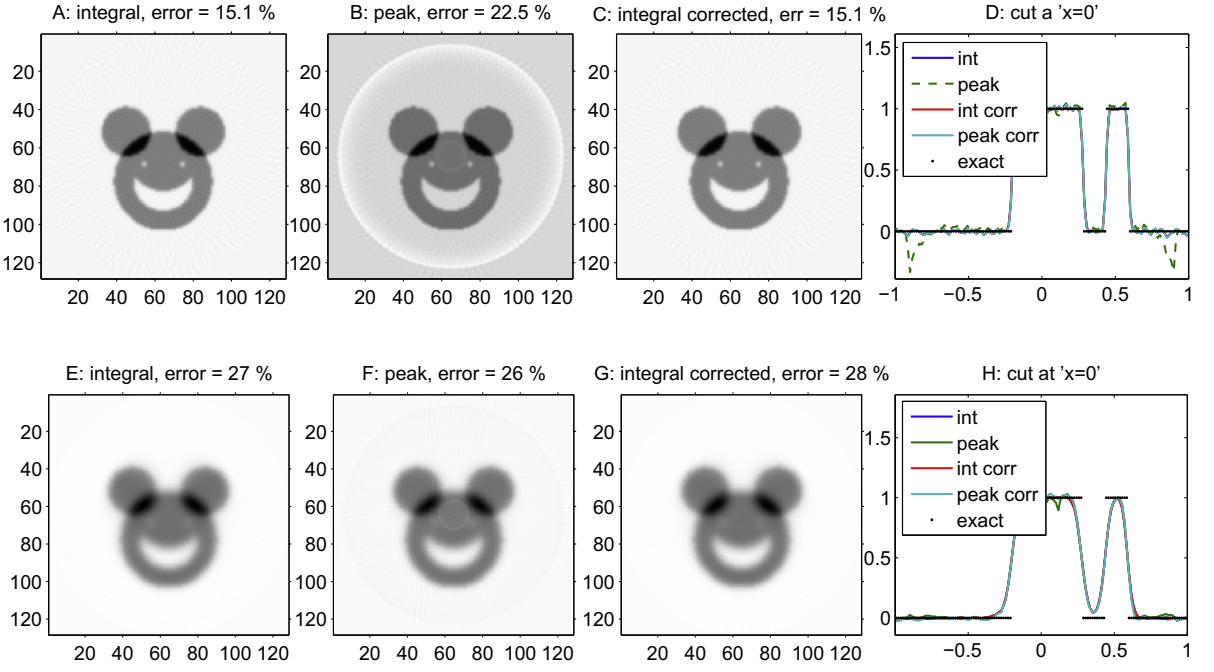


**Fig. 13.** Total attenuation reconstructions with diffusion effects of 'Fermi-Pencil-Beam' type. The coefficient $d$ from formula (38) equals $2.5\,10^{-4}$ in the top row and $2.5\,10^{-3}$ in the bottom row. Errors are relative $L^2$. (a) and (e): reconstructions using formula (54). (b) and (f): reconstructions using formula (53). (c) and (g): reconstructions using formula (55) (very similar results to (56)). (d) and (h): cross section at $x = 0$ for all reconstruction formulas. All formulas give very similar results, and give a regularized version of the total attenuation coefficient, all the more regularized that $d$ is large. We observe artifacts at the boundary of the domain for formula (53) when diffusion is small.

For $1 \leqslant j \leqslant n$, we find that

$$\mathcal{A}_1(r_i, \theta_{\text{in}}; r_{ij}, \theta_{\text{out}}) = \frac{I_{\text{in}}}{\sin\alpha} E_\sigma\left(x_i^-, x_{ij}, x_{ij}^+\right) k(x_{ij}, \theta_{\text{in}}, \theta_{\text{out}}). \tag{58}$$

Here, $E_\sigma\left(x_i^-, x_{ij}, x_{ij}^+\right)$ is the inverse of the exponential of the broken line integral of $\sigma$ along $\left[x_i^-, x_{ij}, x_{ij}^+\right]$. This broken line integral is estimated numerically by a standard quadrature rule using the absorption map $\sigma(x)$ constructed from $\mathcal{A}_0$. This provides a first formula for $k$ given by

$$k(x_{ij}, \theta_{\text{in}}, \theta_{\text{out}}) = \sin\alpha \frac{\mathcal{A}_1(r_i, \theta_{\text{in}}; r_{ij}, \theta_{\text{out}})}{I_{\text{in}} E_\sigma\left(x_i^-, x_{ij}, x_{ij}^+\right)}. \tag{59}$$

The numerical integration of $E_\sigma$ may be avoided again by a calibration technique. Let us define the single scattering contribution obtained with a scattering coefficient $k \equiv 1$:

$$\mathcal{A}_{1,k\equiv 1}(r_i, \theta_{in}; r_{ij}, \theta_{out}) = \frac{I_{\text{in}}}{\sin\alpha} E_\sigma\left(x_i^-, x_{ij}, x_{ij}^+\right).$$

Then, a natural formula for the reconstruction of $k$ that is quite insensitive to discretization effects is given by:

$$k(x_{ij}, \theta_{\text{in}}, \theta_{\text{out}}) = \frac{\mathcal{A}_1(r_i, \theta_{\text{in}}; r_{ij}, \theta_{\text{out}})}{\mathcal{A}_{1,k\equiv 1}(r_i, \theta_{\text{in}}; r_{ij}, \theta_{\text{out}})}. \tag{60}$$

In our numerical simulations, we saw fairly minor differences between the reconstructions because our scattering coefficient is chosen to be smooth. In particular, the error in the $L^2$ norm is relatively insensitive to the method that we use. Still, the second formula tends to produce smoother reconstructions. Fig. 14 illustrates these statements.

*5.3.1. Impact of the angle $\alpha = \theta_{\text{out}} - \theta_{\text{in}}$*

In our numerical simulations, the physical size of the support of the ballistic part is equal to $2 = |\,[-1, 1]\,|$. The cone of lines emitted with direction $\theta_{\text{out}}$ has a trace on $\Gamma_{+,\theta_{\text{out}}}$ with support of size bounded by $2\sin\alpha$; see Fig. 15. The compression is therefore quite severe when $\alpha$ is close to 0. The information on $k$ encoded on $n$ pixels along the ballistic part is therefore shrunk to

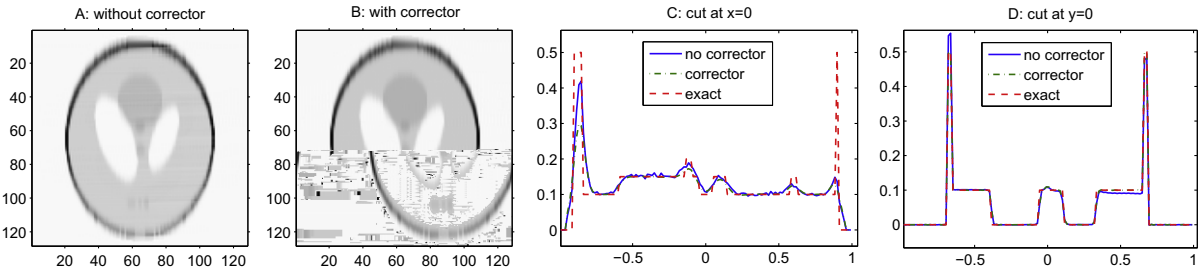


**Fig. 14.** Scattering reconstructions when Gaussian beams of width $2.5h$ ($h$ the step-size) are sent instead of Dirac pulses. Formula (59) does not take into account the beam width, hence the numerical artifacts (horizontal lines) in image (a). These artifacts vanish with formula (60) (image (b)), though the $L^2$ errors remain similar. Plots (c) and (d) show cross sections of both reconstructions.

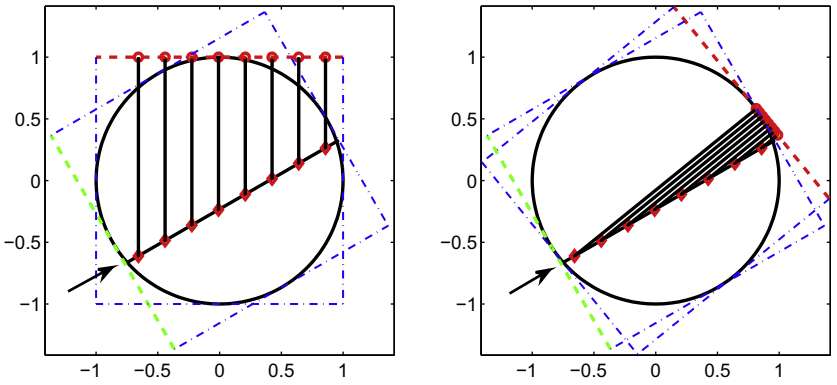

**Fig. 15.** Geometry for the single scattering. Legend: ∘: measurement points; ♢: reconstruction points; →: input. Left: a favorable case with $\alpha = \frac{\pi}{3}$. Right: a less favorable case with $\alpha = \frac{\pi}{20}$.

information encoded over $n \sin\alpha$ pixels at best. High frequencies in $k$ are therefore irretrievably lost and even low frequencies component are lost when $\alpha$ tends to 0 until only the spatial average of $k$ is available and (60) fails to adequately reconstruct the scattering coefficient. The resolution clearly improves when $n$ increases at a fixed value of $\alpha$ since we can roughly reconstruct $n \sin\alpha$ Fourier modes of $k$ along the segment $t \mapsto x_{\text{in}} + t v_{\text{in}}$. But loss in resolution is unavoidable when $\alpha$ is small. The most favorable situation is obviously $\sin\alpha = 1$, which should clearly be chosen to reconstruct $k = k(x)$ independent of the angular variables.

Since $\theta_{\text{out}} \neq \theta_{\text{in}}$, the ballistic part needs to be rotated first in order for $\theta_{\text{out}}$ to be aligned with one of the grid axes. Such a rotation may induce strong oscillations of the source term in the transport equation and generate oscillations on the single scattering measurements. We have observed that such effects were amplified when $\alpha$ was small. A solution to such numerical instabilities is to send regularized (Gaussian beams) on $\Gamma_-$ or to have angular diffusion in order to regularize the ballistic term. Fig. 16 shows how the reconstruction degrades when $\alpha$ decreases.

### 5.3.2. Different scattering scenarios

In the most general case, when $k \equiv k(x, \theta_{\text{in}}, \theta_{\text{out}})$ depends non trivially on $\theta_{\text{in}}$ and $\theta_{\text{out}}$, the above formulas (59) and (60) can hardly be improved. In many practical settings, $k \equiv k(x, v_{\text{in}} \cdot v_{\text{out}})$ depends only on the difference of the two angles $\theta_{\text{in}}$ and $\theta_{\text{out}}$. This situation arises when scattering is isotropic, i.e., when scattering is independent of rotations of the configuration domain. Such assumptions are sometimes violated, for instance in absorption and scattering through canopy, but are valid in many practical settings of medical and geophysical imaging. The reconstructions in (59) and (60) may then be improved by averaging over angles, e.g.

$$k(x_{ij}, \theta_{\text{in}}, \theta_{\text{out}}) = \int_0^{2\pi} \frac{\mathcal{A}_1(r_i, \theta_{\text{in}} + \phi; r_{ij}, \theta_{\text{out}} + \phi)}{\mathcal{A}_{1,k\equiv 1}(r_i, \theta_{\text{in}} + \phi; r_{ij}, \theta_{\text{out}} + \phi)} \frac{d\phi}{2\pi}. \tag{61}$$

Here, $r_i$ and $r_{ij}$ depend implicitly on $\phi$ by replacing $\theta_{\text{in}}$ and $\theta_{\text{out}}$ by $\theta_{\text{in}} + \phi$ and $\theta_{\text{out}} + \phi$, respectively. Averaging over only two directions already yield some reasonable gains in the reconstructions as may be seen in Fig. 17. When $k = k(x)$ is independent of angles, then the choice $\alpha = \frac{\pi}{2}$ and $\theta_{\text{in}} = 0$ is optimal.

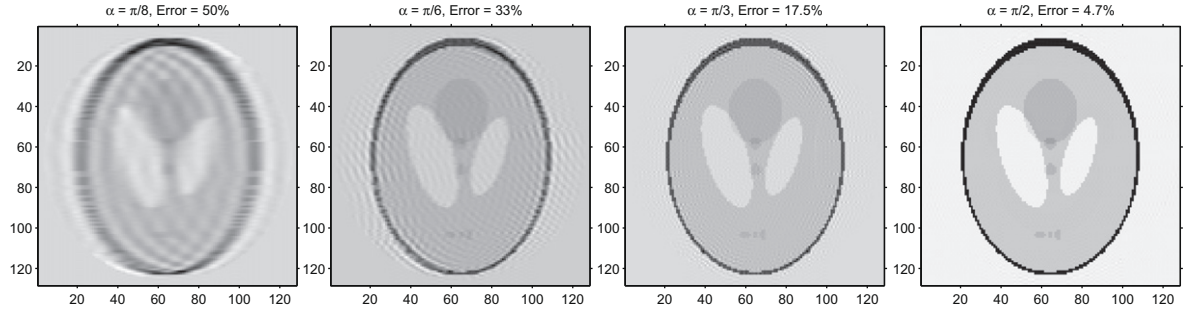


**Fig. 16.** Quality of scattering reconstructions versus deviation angle $\alpha$. From left to right, $\theta_{\text{out}} - \theta_{\text{in}} = \frac{\pi}{8}, \frac{\pi}{6}, \frac{\pi}{3}$ and $\frac{\pi}{2}$ (best case). Errors are relative $L^2$ and $\theta_{in} = \frac{\delta}{2}$.

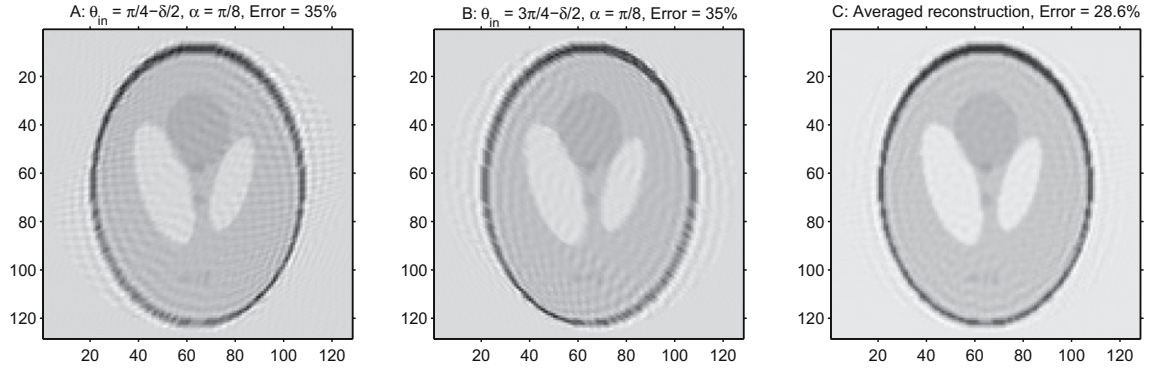


**Fig. 17.** Averaging over a few scattering reconstructions for $\theta_{\text{out}} - \theta_{\text{in}} = \frac{\pi}{8}$. Images (a) and (b) show reconstructions from single, different configurations $\theta_{\text{in}}, \theta_{\text{out}}$, and present strong oscillations along their respective $\theta_{\text{in}}$-axes. Image (c) is averaged over seven reconstructions with $\theta_{\text{in}} = i\frac{\pi}{4} - \frac{\delta}{2}$, $i = 1, \ldots, 7$. Errors are relative $L^2$.

### 5.4. Iterative reconstruction of the optical parameters

We now return to the iterative algorithm briefly mentioned at the end of Section 5.1. The previous sections show how $\sigma(x)$ and $k(x,\theta',\theta)$ may be reconstructed from knowledge of $\mathcal{A}_0$ and $\mathcal{A}_1$. It remains to calculate the latter terms from knowledge of the full operator $\mathcal{A}$. This may be done iteratively for sufficiently small values of $k$ in two space dimensions and for sufficiently small noise as is e.g. justified in [11,30]. The reason why this may be done is that $\mathcal{A}-\mathcal{A}_0$ and $\mathcal{A}-\mathcal{A}_1$ can be estimated numerically by solving a transport equation once $\sigma(x)$ and $k(x,\theta',\theta)$ are known approximately. Knowledge of $\mathcal{A}$ and of $\mathcal{A}-\mathcal{A}_k$ obviously gives us knowledge of $\mathcal{A}_k$ for $k=0,1$. More formally, the iterative algorithm is structured as follows.

Let us denote the full measurement data by

$$D := \mathcal{A}_0(\sigma) + \mathcal{A}_1(\sigma,k) + \mathcal{A}_2(\sigma,k).$$

Let us further denote formally by $\mathcal{A}_0^{-1}$ any of the reconstruction formulas that give us an approximation of $\sigma$ from the ballistic measurements $\mathcal{A}_0(\sigma)$ (this involves one of the formulas (53)–(55) or (56), followed by an Inverse Radon Transform), and by $\mathcal{A}_1^{-1,\sigma}$, any of the reconstruction formulas that reconstruct $k$ from the single scattering measurements $\mathcal{A}_1(\sigma,k)$. Then we can write the following

$$\sigma \approx \mathcal{A}_0^{-1}\mathcal{A}_0(\sigma) = \mathcal{A}_0^{-1}(D - \mathcal{A}_1(\sigma,k) - \mathcal{A}_2(\sigma,k)).$$
$$k \approx \mathcal{A}_1^{-1,\sigma}\mathcal{A}_1(\sigma,k) = \mathcal{A}_1^{-1,\sigma}(D - \mathcal{A}_0(\sigma) - \mathcal{A}_2(\sigma,k)).$$

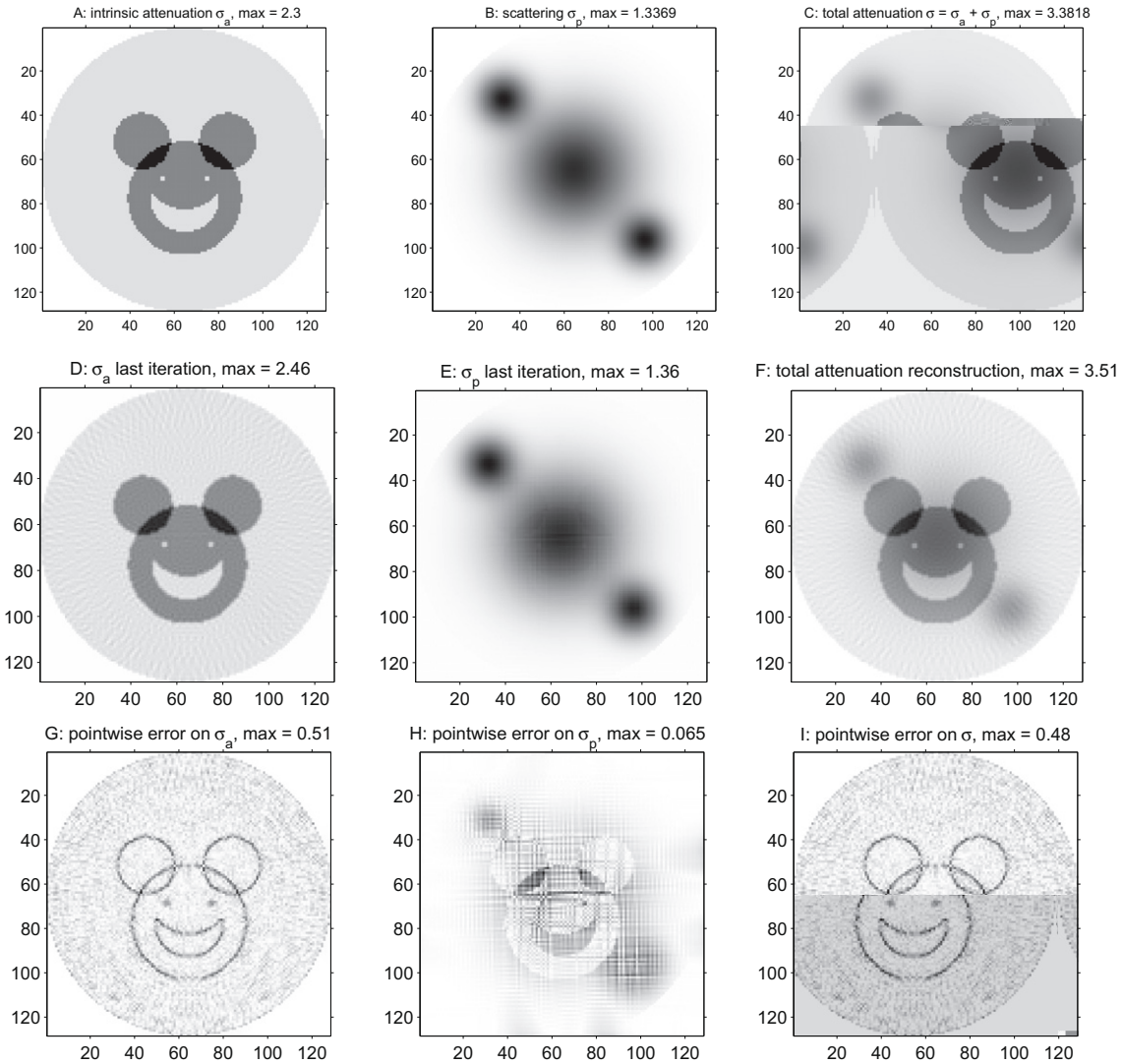


**Fig. 18.** Iterated scattering reconstruction. Sub-plots (a), (b) and (c) show the exact parameters. Sub-plots (d) and (e) show the reconstructions of $\sigma_a$ and $\sigma_p$ after convergence of the iterative scheme, while sub-plot (f) shows the reconstruction of the total attenuation. The last row displays point-wise errors for all coefficients $\sigma_a, \sigma_p$ and $\sigma$.

Assuming that the operators in both right-hand sides are contractions, then iterating over these operators with good initial guesses should converge to improved reconstructions of both optical parameters. The iterative scheme reads as follows:

$$\begin{aligned}&\sigma_0 = \mathcal{A}_0^{-1} D, \quad k_0 = \mathcal{A}_1^{-1,\sigma_0} D,\\ &\sigma_{l+1} = \mathcal{A}_0^{-1}(D - \mathcal{A}_1(\sigma_l) - \mathcal{A}_2(\sigma_l, k_l)),\\ &k_{l+1} = \mathcal{A}_1^{-1,\sigma_{l+1}}(D - \mathcal{A}_0(\sigma_l) - \mathcal{A}_2(\sigma_l, k_l)).\end{aligned} \tag{62}$$

Theoretical results show that the above operators are indeed contractions at the continuous level (i.e., before spatial and angular discretizations) and in the absence of noise (i.e., no angular diffusion) independent of $k$ in dimension $d \geqslant 3$ and for small $k$ in dimension $d = 2$. It is highly likely though not proved rigorously mathematically that the algorithm is also a contraction when the angular diffusion is small (see e.g. [11]) and the grid size $h = \frac{2}{n}$ and angular size $\delta$ are sufficiently small.

In the numerical simulations presented below, we assume that the scattering kernel is a function of position only (i.e., $k(x, \theta, \theta') = k(x)$) and we define the quantity

$$\sigma_{\mathrm{p}}(x) := \int_{\mathbb{S}^1} k(x)\, d\theta = 2\pi k(x).$$

Thus, $\sigma_{\mathrm{p}}$ is the scattering contribution to the total attenuation with $\sigma(x) = \sigma_{\mathrm{a}}(x) + \sigma_{\mathrm{p}}(x)$, where $\sigma_{\mathrm{a}}$ is the intrinsic absorption. We are interested in a situation where the intrinsic attenuation may have jump discontinuities and/or localized inclusions and the scattering coefficient is smoother, see Fig. 18(a)–(c). In such a setting and with relatively small angular blurring, the single and multiple scattering contributions hardly affect the measurements of $\mathcal{A}_0$. In other words, on the support of $\mathcal{A}_0$, the remainder $\mathcal{A} - \mathcal{A}_0$ is rather small. As a consequence, our strategy to recover the optical parameters $\sigma_{\mathrm{a}}(x)$ and $k(x)$, or equivalently $\sigma_{\mathrm{a}}(x)$ and $\sigma_{\mathrm{p}}(x)$, is as follows: we first compute the total attenuation $\sigma(x)$ by applying $\mathcal{A}_0^{-1}$ to the full measurement data $D$. We then reconstruct $k(x)$ using the iterative scheme that can be deduced from (62). At each iteration, we estimate the terms $\sigma_{\mathrm{p}}$ and $\sigma_{\mathrm{a}}$ as

$$\sigma_{\mathrm{p},l} = 2\pi k_l, \qquad \sigma_{\mathrm{a},l} = \sigma - \sigma_{\mathrm{p},l}, \qquad l = 0, \ldots, N_{\mathrm{iter}}.$$

The iterative scheme thus reads:

$$\begin{aligned}&\sigma = \mathcal{A}_0^{-1} D, \quad k_0 = \mathcal{A}_1^{-1,\sigma} D,\\ &k_{l+1} = \mathcal{A}_1^{-1,\sigma}(D - \mathcal{A}_0(\sigma) - \mathcal{A}_2(\sigma, k_l)) = k_0 - \mathcal{A}_1^{-1,\sigma}(\mathcal{A}_0(\sigma) + \mathcal{A}_2(\sigma, k_l)).\end{aligned} \tag{63}$$

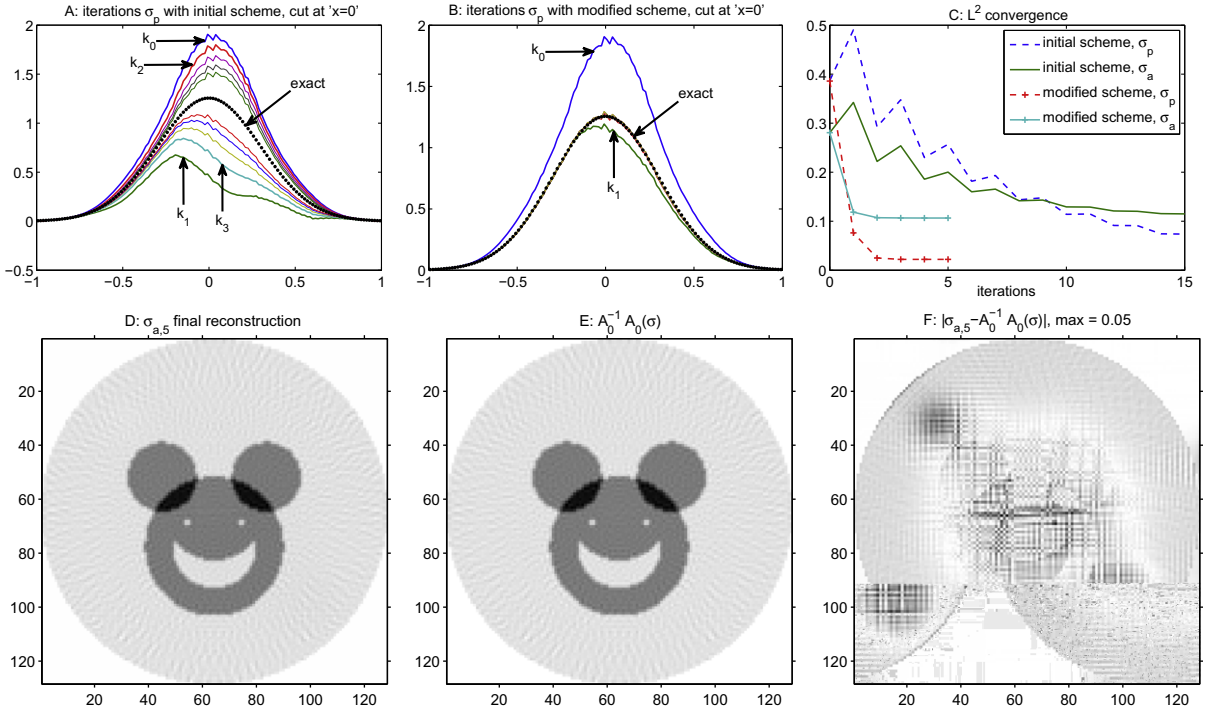


**Fig. 19.** Remarks on the convergence. Plot (a) shows a cross section of iterations of the scattering coefficient using the initial oscillatory scheme. Plot (b) shows the same iterations using the modified scheme (64) with $\beta = \frac{1}{2}$. Plot (c) displays $L^2$ convergence of both iterative schemes. The second row compares the reconstructed intrinsic absorption with $\mathcal{A}_0^{-1}\mathcal{A}_0(\sigma_{\mathrm{a}})$.

The iterative scheme converges rather slowly and oscillates about its limit. Since measurements include multiple scattering and the first reconstruction $k_0$ of the scattering map is based on single scattering, the latter is overestimated. The forward map then also overestimates the influence of multiple scattering in the data and thus removes "too much" multiple scattering for the next reconstruction $k_1$ of the scattering map, which is therefore smaller than the true map, and so on. Even iterates of $k_l$ therefore overestimate the true scattering map while odd iterates of $k_l$ underestimate it. More formally, the equality

$$k_{l+1} - k_l = -\mathcal{A}_1^{-1,\sigma}(\mathcal{A}_2(\sigma, k_l) - \mathcal{A}_2(\sigma, k_{l-1})),$$

shows the change of sign of $k_{l+1} - k_l$ at each iteration since $\mathcal{A}_2$ is monotonically increasing in its arguments. To reduce these oscillations and accelerate the convergence, we need a scheme that better utilizes previous iterations, for instance the following relaxation scheme

$$k_{l+1} = \beta\Big(\mathcal{A}_1^{-1,\sigma} D - \mathcal{A}_1^{-1,\sigma}(\mathcal{A}_0(\sigma) + \mathcal{A}_2(\sigma, k_l))\Big) + (1-\beta)k_l, \tag{64}$$

for some $\beta \in (0,1)$. Numerical results with the value $\beta = \frac{1}{2}$ show that this scheme indeed converges quite rapidly; compare Fig. 19, plots (a) and (b).

*5.4.1. Numerical reconstruction in the absence of angular blurring*

In all simulations, we have $n = N_d = 128$. The reconstruction settings for the scattering coefficient are: $\theta_{in} = \frac{\delta}{2}$ (i.e., the incoming direction is very close to $e_x$; this maximizes the numerical effects of the rotation), $\alpha = \theta_{\text{out}} - \theta_{\text{in}} = \frac{\pi}{2}$, inputs are Dirac pulses. In a first numerical experiment, we assume no angular diffusion. The forward simulation is obtained by computing scattering terms up to order five.

As in Section 5.2, the total attenuation is reconstructed using an inverse Radon Transform (IRT). The error is mainly localized at the discontinuities (see Fig. 18(d)). The modified iterative scheme (64) converges after 3–4 iterations and we achieve a relative error of 2.2% on $\sigma_{\text{p}}$ and 10.6% on $\sigma_{\text{a}}$ (see point-wise errors on Fig. 18(g) and (h)). The error on the reconstruction of the intrinsic attenuation map is therefore similar to the setting obtained earlier in the absence of scattering.

The reconstruction contains two main sources of error: the error caused by the Inverse Radon Transform (IRT), and the error caused by the non-ballistic part of the measurements (which were neglected at first). In a discrete setting, the IRT does not recover singularities well and creates radial artifacts caused by the angular discretization. Thus, $\mathcal{A}_0^{-1}\mathcal{A}_0(\sigma) - \sigma$ presents peaks close to the singularities of $\sigma$ as well as radial noise. Since the iterative scheme uses $\mathcal{A}_0^{-1}\mathcal{A}_0(\sigma)$ and scattering is smooth with $\mathcal{A}_0^{-1}\mathcal{A}_0(\sigma_{\text{p}}) \approx \sigma_{\text{p}}$ a good approximation, the iterations on the intrinsic absorption should provide a much better approximation for $\mathcal{A}_0^{-1}\mathcal{A}_0(\sigma_{\text{a}})$ than for $\sigma_{\text{a}}$. We indeed observe that the relative $L^2$-error of $\sigma_{\text{a},5}$ with respect to $\mathcal{A}_0^{-1}\mathcal{A}_0(\sigma_{\text{a}})$ is 1.4%. Fig. 19(f) shows that the errors are no longer as localized near the singularities unlike Fig. 18(g), where we display $|\sigma_{\text{a},5} - \sigma_{\text{a}}|$. We do notice some of the scattering coefficient in that error plot, in the same way that we notice some intrinsic absorption in the scattering reconstruction error in Fig. 18(h). This cross-over in the reconstructions is probably unavoidable. However, it is significantly smaller than the error we expect when we apply the IRT. In this sense, the iterative reconstruction algorithm successfully separates the intrinsic attenuation and scattering components of the total attenuation map.

*5.4.2. Numerical reconstruction with angular blurring*

We now consider the framework where the ballistic part is blurred by some Fermi pencil beam transverse diffusion with a constant coefficient $d = 2.5\,10^{-4}$ in formula (38). Fig. 21(a) displays how the beam widens as it passes through the center of the domain. We still compute full measurements using five scattering terms in the forward solver. We then reconstruct the total absorption coefficient $\sigma$ by using formula (56). In other words, we assume that the physical measurements are given to us by $\frac{\int_{-1}^{1} \mathcal{A}_0(r_i,\theta_j;r,\theta_j)\,dr}{\int_{-1}^{1} \mathcal{A}_{0,d}(r_i,\theta_j;r,\theta_j)\,dr}$, which corresponds to a faithful approximation of the physical blurred measurements that depends very little on the discretization used in the simulations. The reconstruction of $\sigma_{\text{p}}$ and $\sigma_{\text{a}}$ is performed using the modified scheme (64).

The results are gathered in Fig. 20. As in the absence of angular blurring, we observe that the scattering coefficient is reconstructed accurately. The smoothness of the latter coefficient makes the reconstructions quite robust with respect to angular diffusion. Note also that the coefficient $E_\sigma$ appearing in the reconstruction of the scattering coefficient is estimated more accurately than $\sigma$ itself because it involves (broken) line integrals of $\sigma$, which are more robust with respect to noise than point-wise estimates.

Errors on $\sigma = \sigma_{\text{a}} + \sigma_{\text{p}}$ are therefore inherited by the intrinsic attenuation coefficient $\sigma_{\text{a}}$. The reconstructed coefficient $\sigma_{\text{a}}$ unsurprisingly has smoother edges than in the case without diffusion. Hence the larger error at the edges, see Fig. 18(g) and Fig. 20(d). As in the case without diffusion, we notice that $\sigma_{\text{a}}$ actually converges to the function $\sigma_{\text{a}}^{k=0} \equiv \mathcal{A}_0^{-1}\mathcal{A}_0(\sigma_{\text{a}})$, which is what we would reconstruct from ballistic measurements with angular diffusion and no scattering; see Fig. 21, where we observe a relative $L^2$ error of 1.4%.

To conclude this section, we would like to stress that the iterative algorithm accurately separates the scattering and intrinsic attenuation components of the total attenuation coefficient also in the presence of small angular diffusion. Whether we pick a reconstruction formula that requires knowledge of noise a priori or not, a smooth scattering coefficient is always reconstructed well, whereas the intrinsic attenuation inherits the imperfections of the reconstruction formula for the total attenuation, may these imperfections come from the inverse Radon Transform or from the inaccurate estimation of the numerical noise. Finally, let us insist on the fact that even in the setting where noise is known, the above results show

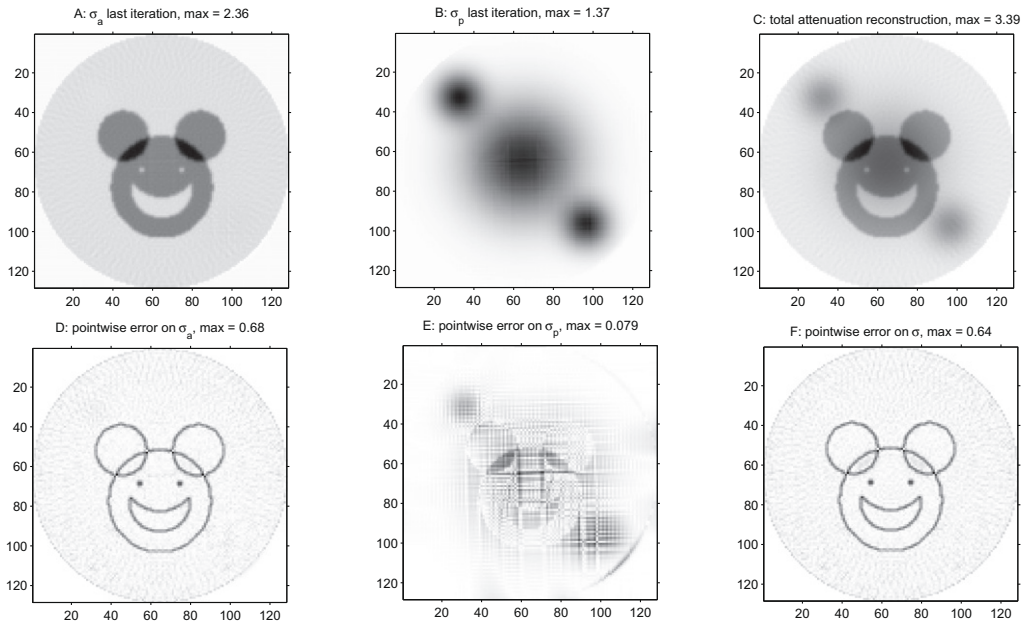


**Fig. 20.** Results of reconstructions. The exact coefficients in Fig. 18, first row. Relative $L^2$ errors drop from 39% to 2.2% in three iterations for $\sigma_p$, and from 28% to 11% for $\sigma_a$.

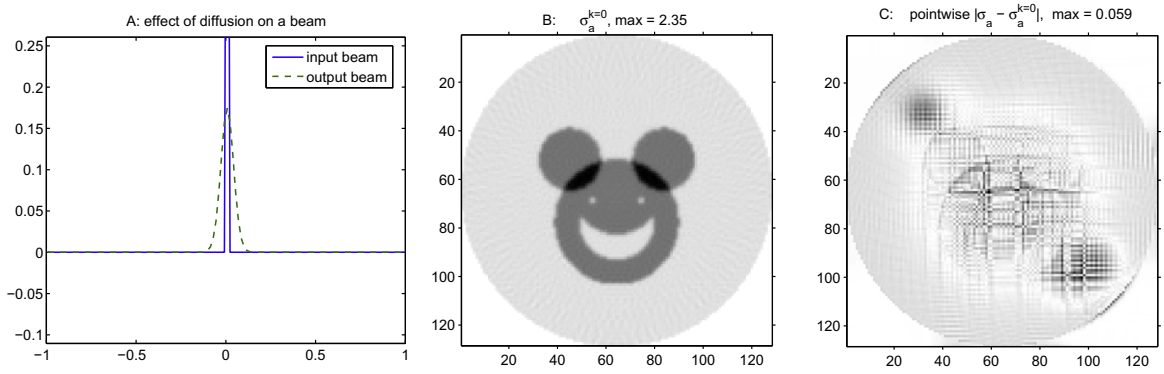


**Fig. 21.** Remarks on the simulation with blurring.

how the discontinuities are blurred in the reconstructions, and irretrievably so in the absence of prior knowledge about the objects we wish to reconstruct.

*5.4.3. Summary of algorithmic complexity and parallelizability*

Let us conclude this section by a summary of the various computational costs of the forward and inverse transport codes. We recall the notation; $n$: the size of the reconstructed (square) image; $N_d$: number of directions in the discretization of $\mathbb{S}^1$; $N_{\text{scat}}$: number of scattering terms that we compute when solving a forward transport problem; $N_{\text{iter}}$: number of iterations in the iterative reconstruction scheme (62); $N_{\text{avg}}$: number of scattering reconstructions over which we average in order to get better accuracy.

The complexities of the numerical algorithms presented in this paper are summarized as follows:

- a single propagation of ray along the grid requires $\mathcal{O}(n^2)$ operations and an image rotation, $\mathcal{O}(n^2 \log n)$ operations.
- solving a forward problem for one given input requires one ballistic propagation and $N_d N_{\text{scat}}$ scattering propagations, so it requires $\mathcal{O}((1 + N_{\text{scat}} N_d) n^2 \log n)$ operations. Creating full measurements requires solving a forward problem for each input pulse at position $(r_i, \theta_j)$, hence measurements have a computational cost of $\mathcal{O}(n N_d (1 + N_{\text{scat}} N_d) n^2 \log n)$.
- In the most general case of scattering, all iterative schemes require the computation of full measurements at each iteration, so the iterative reconstruction will be of the order $\mathcal{O}(N_{\text{iter}} n N_d (1 + N_{\text{scat}} N_d) n^2 \log n)$. When the scattering is only function of position $k(x)$, it can be reconstructed from measurements with only one input direction, which reduces the latter cost by a factor $N_d$.

In the presence of parallel architectures and the availability of $p \times N_d$ processors, $1 \leqslant p \leqslant n \times N_d$, the total computational time may be reduced by a factor close to $p \times N_d$. Creating the measurement operator requires that we run $n \times N_d$ independent forward solvers. For each of these solvers, one step of the iterated source method requires $N_d$ independent solutions of the free transport equation. Hence the strategy with $p \times N_d$ processors is to create $p$ groups of $N_d$ processors. Each group can then run a forward solver with complexity $\mathcal{O}((1 + N_{\text{scat}})n^2 \log n)$ (instead of $\mathcal{O}((1 + N_{\text{scat}}N_d)n^2 \log n)$ on a single processor). We then create the full measurements by splitting the $n \times N_d$-long loop over the $p$ groups of processors. Neglecting communications, which should be minimal in practice for sufficiently large spatial domains, we obtain a gain of time $p \times N_d$ provided the latter number of processors is available.

## 6. Conclusions

This paper presents a numerical methodology to solve the inverse transport problem, which consists of reconstructing the optical parameters in a transport equation from full knowledge of the albedo operator. The main message that can be drawn from the mathematical analysis of the inverse transport problem is that reconstructions of the optical parameters are stable when the singular structure of the albedo operator can be used. This requires that the singularities of the forward transport operator be estimated accurately, a task that is difficult to do on a Cartesian grid because of the hyperbolic structure of the transport equation.

The method based on slanting or fully rotating the computational domain to solve the free transport equation allows one to devise a Cartesian-friendly method that accurately captures the ballistic and single scattering components of the transport solution. The equation after rotation is sufficiently simple that various physical blurring effects such as those caused by angular diffusion can be accounted for. The numerical tool we have presented then allows one to understand what can and cannot be reconstructed in an object of interest based on various measurement configurations. We have presented numerical reconstructions based on full knowledge of the ballistic part and full knowledge of scattering for the angle $\theta_{\text{out}} - \theta_{\text{in}} = \frac{\pi}{2}$. In this setting, the separation of a smooth scattering coefficient from a more singular absorption coefficient, which is an interesting configuration in practice, was shown to be performed accurately.

The methodology easily generalizes to the three dimensional transport equation, where polarization effects such as those described in [13] can also be included. The computational cost of the method however becomes quite high. The price to pay for the rotations is unavoidable if some spectral accuracy in the rotations is to be maintained. More local interpolants can also be developed to account for the rotations and this is being considered elsewhere. The setting based on rotations is however fairly robust as it allows one to account for several physical blurring mechanisms relatively painlessly. The total computational cost of the method is however an issue. It can be reduced significantly by carefully analyzing the singularities of the transport solution. For instance, contributions for high orders of scattering are much smoother than the ballistic contribution. They can therefore be captured by spatial and angular grids that are much coarser than the grid used for the ballistic part. Multi-grid and Sparse techniques (see e.g. [32]) might then be used to reduce the computational cost of the method, which is arguably quite high.

## Acknowledgment

This work was supported in part by NSF Grants DMS-0554097 and DMS-0804696.

## References

[1] M.L. Adams, E.W. Larsen, Fast iterative methods for deterministic particle transport computations, Prog. Nucl. Energy 40 (2002) 1–159.
[2] R.E. Alcouffe, Diffusion synthetic acceleration methods for the diamond-differenced discrete-ordinates equations, Nucl. Sci. Eng. 64 (1977) 344.
[3] V.S. Antyufeev, A.N. Bondarenko, X-ray tomography in scattering media, SIAM J. Appl. Math. 56 (1996) 573–587.
[4] S.R. Arridge, Optical tomography in medical imaging, Inverse Prob. 15 (1999) R41–R93.
[5] A. Averbuch, R.R. Coifman, D.L. Donoho, M. Israeli, J. Waldén, Fast Slant Stack: A Notion of Radon Transform for Data in a Cartesian Grid which is Rapidly Computible, Algebraically Exact, Geometrically Faithful and Invertible, preprint.
[6] A. Averbuch, R.R. Coifman, D.L. Donoho, M. Israeli, J. Waldén, The Pseudopolar FFT and its Applications, preprint.
[7] D.H. Bailey, P.N. Swarztrauber, The fractional Fourier transform and applications, SIAM Rev. 33 (1991) 389–404.
[8] G. Bal, Fourier analysis of the diamond discretization in particle transport, Calcolo 38 (3) (2001) 141–172.
[9] G. Bal, Inverse transport theory and applications, Inverse Prob. 25 (2009) 053001.
[10] G. Bal, A. Jollivet, Stability estimates in stationary inverse transport, Inverse Prob. Imaging 2 (4) (2008) 427–454.
[11] G. Bal, A. Jollivet, Approximate stability in inverse transport, Y. Censor, M. Jiang, G. Wang (Eds.), Biomedical Mathematics: Promising Directions in Imaging, Therapy Planning and Inverse Problems, Medical Physics Publishing, Madison, WI, USA, in press.
[12] G. Bal, P. Moireau, Fast numerical inversion of the attenuated Radon transform with full and partial measurements, Inverse Prob. 20 (4) (2004) 1137–1164.
[13] S. Chandrasekhar, Radiative Transfer, Dover Publications, New York, 1960.
[14] A. Charette, J. Boulanger, H.K. Kim, An overview on recent radiation transport algorithm development for optical tomography imaging, J. Quant. Spectrosc. Radiat. Transfer. 109 (2008) 2743–2766.
[15] M. Choulli, P. Stefanov, An inverse boundary value problem for the stationary transport equation, Osaka J. Math. 36 (1999) 87–104.
[16] R. Dautray, J.-L. Lions, Mathematical Analysis and Numerical Methods for Science and Technology, vol. 6, Springer Verlag, Berlin, 1993.
[17] B. Després, F. Lagoutière, Generalized harten formalism and longitudinal variation diminishing schemes for linear advection on arbitrary grids, M2AN Math. Model. Numer. Anal. 35 (2001) 1159–1183.
[18] H. Gao, H. Zhao, A fast forward solver of radiative transfer equation, Transp. Theory Stat. Phys. 38 (2009) 149–192.
[19] C. Johnson, J. Pitkäranta, An analysis of the discontinuous Galerkin method for a scalar hyperbolic equation, Math. Comput. 46 (173) (1986) 1–26.

[20] E.W. Larsen, Unconditionally stable diffusion–acceleration of the transport equation, Transp. Theory Stat. Phys. 11 (1982) 29–52.
[21] C.L. Leakeas, E.W. Larsen, Generalized Fokker Planck approximations of particle transport with highly forward-peaked scattering, Nucl. Sci. Eng. 137 (2001) 236–250.
[22] E.E. Lewis, W.F. Miller Jr., Computational Methods of Neutron Transport, J. Wiley and sons, New York, 1984.
[23] X.D. Liu, S. Osher, T. Chan, Weighted essentially nonoscillatory scheme, J. Comput. Phys. 115 (1) (1994) 200–212.
[24] I. Lux, L. Koblinger, Monte Carlo Particle Transport Methods: Neutron and Photon Calculations, CRC Press, Boca Raton, 1991.
[25] T.A. Manteuffel, K. Ressel, Least-squares finite-element solution of the neutron transport in diffusive regimes, SIAM J. Numer. Anal. 35 (2) (1998) 806–853.
[26] K.A. Mathews, On the propagation of rays in discrete ordinates, Nucl. Sci. Eng. 132 (1999) 155–180.
[27] M. Mokhtar-Kharroubi, Mathematical Topics in Neutron Transport Theory, World Scientific, Singapore, 1997.
[28] F. Natterer, The Mathematics of Computerized Tomography, Wiley, New York, 1986.
[29] K. Ren, G. Bal, A.H. Hielscher, Frequency domain optical tomography based on the equation of radiative transfer, SIAM J. Sci. Comput. 28 (2006) 1463–1489.
[30] P. Stefanov, G. Uhlmann, Optical tomography in two dimensions, Methods Appl. Anal. 10 (2003) 1–9.
[31] J.-N. Wang, Stability estimates of an inverse problem for the stationary transport equation, Ann. Inst. Henri Poincaré 70 (1999) 473–495.
[32] G. Widmer, R. Hiptmair, C. Schwab, Sparse adaptive finite elements for radiative transfer, J. Comput. Phys. 12 (2008) 6071–6105.